

See discussions, stats, and author profiles for this publication at: <https://www.researchgate.net/publication/263958970>

# Correlation between Accurate Electron Density and Linear Optical Properties in Amino Acid Derivatives: L-Histidinium Hydrogen Oxalate

ARTICLE in CRYSTAL GROWTH & DESIGN · JUNE 2013

Impact Factor: 4.89 · DOI: 10.1021/cg400411t

CITATIONS

6

READS

53

5 AUTHORS, INCLUDING:



[Marlena Gryl](#)

Jagiellonian University

22 PUBLICATIONS 58 CITATIONS

SEE PROFILE



[Anna Krawczuk](#)

Jagiellonian University

18 PUBLICATIONS 68 CITATIONS

SEE PROFILE



[Piero Macchi](#)

Universität Bern

145 PUBLICATIONS 2,219 CITATIONS

SEE PROFILE

# Correlation between Accurate Electron Density and Linear Optical Properties in Amino Acid Derivatives: L-Histidinium Hydrogen Oxalate

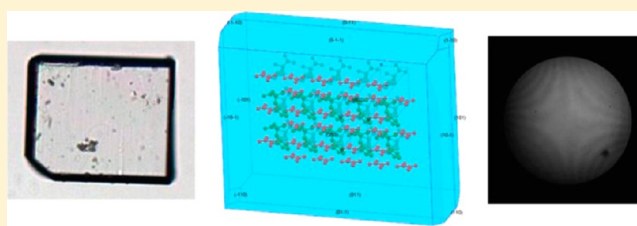
Abita Shyorotra Chimpri,<sup>†</sup> Marlena Gryl,<sup>‡</sup> Leonardo H. R. Dos Santos,<sup>†</sup> Anna Krawczuk,<sup>‡</sup> and Piero Macchi<sup>\*,†</sup>

<sup>†</sup>Department of Chemistry and Biochemistry, University of Bern, Freiestrasse 3, 3012 Bern, Switzerland

<sup>‡</sup>Faculty of Chemistry, Jagiellonian University, Ingardena 3, 30-060 Kraków, Poland

## S Supporting Information

**ABSTRACT:** The accurate electron density and linear optical properties of L-histidinium hydrogen oxalate are discussed. Two high-resolution single crystal X-ray diffraction experiments were performed and compared with density functional calculations in the solid state as well as in the gas phase. The crystal packing and the hydrogen bond network are accurately investigated using topological analysis based on quantum theory of atoms in molecules, Hirshfeld surface analysis, and electrostatic potential mapping. The refractive indices are computed from couple perturbed Kohn–Sham calculations and measured experimentally. Moreover, distributed atomic polarizabilities are used to analyze the origin of the linear susceptibility in the crystal, in order to separate molecular and intermolecular causes. The optical properties are also correlated with the electron density distribution. This compound also offers the possibility to test the *electron density building block* approach for material science and different refinement schemes for accurate positions and displacement parameters of hydrogen atoms, in the absence of neutron diffraction data.



## 1. INTRODUCTION

The hydrogen bond (HB)  $X-H\cdots Y$  is the most important intermolecular interaction, in which an electropositive H atom “intercedes between two electronegative groups X and Y and brings them closer together”.<sup>1</sup> Depending on the nature of X and Y, the bond can be stronger or weaker, with a more or less covalent character.<sup>2</sup> This flexibility is the reason for the large interest received by the HB, an essential component of the structure and function of biological molecules<sup>3</sup> as well as of many inorganic materials.<sup>4</sup> In the HB species, the hydrogen atom might be subjected to dynamic phenomena that are crucial for the (bio)material properties; among these, the most important is the proton transfer, which can be induced by changing the thermodynamic conditions.<sup>5</sup> More efforts are nowadays devoted to material science oriented research on HB crystal species. In this respect, the determination of the accurate electron density distribution is fundamental to fully appreciate the nature of the chemical bonding<sup>6</sup> and the contribution of the HB to the genesis of material properties.

Within a project on the determination of electron density in building blocks<sup>7</sup> of metal organic frameworks,<sup>8</sup> in particular, metal bio-organic frameworks (M-Bio-F),<sup>9</sup> we are studying hydrogen bonded networks formed by amino acids in co-crystals or salts, precursors of the M-Bio-Fs. During this research, we came across an interesting species: L-histidinium hydrogen oxalate (**1**), first characterized at ambient conditions by Prabu et al.<sup>10</sup> **1** has attracted our attention because of its molecular and

supramolecular arrangement. In fact, the imidazole ring assumes a staggered conformation between the  $\alpha$ -amino and the  $\alpha$ -carboxyl groups, which forces alternate segregation of layers formed by L-histidinium helices and hydrogen oxalate chains. The structure is characterized by several hydrogen bonds, three of them are particularly important: (1)  $O-H\cdots O$  between hydrogen-oxalates (originating the hydrogen oxalate chains); (2)  $N-H\cdots O$  between two L-histidinium ions through imidazole nitrogen and carboxylic oxygen (which produce the L-histidinium helices, further reinforced by weaker  $N-H\cdots O$  bonds through the ammonium group); (3)  $N-H\cdots O$  between the ammonium group of L-histidinium and the hydrogen oxalate (which links the chain and the helices). Interestingly, the two shorter bonds are the homoionic, i.e., the interanionic  $O-H\cdots O$  and the intercationic  $N-H\cdots O$ . There are no short interactions linking two hydrogen oxalate chains or two L-histidinium helices, so that the alternating layers in the crystal are only weakly bound.

Apart from having an interesting HB pattern, L-histidinium hydrogen oxalate belongs to the family of amino acids salts, which have attracted interest for their linear and nonlinear optical properties and their potential applications as functional materials.<sup>11</sup> Recently, there was much progress in the preparation of large size crystals and the applications of these organic

Received: March 20, 2013

Revised: May 14, 2013

Published: June 7, 2013

materials which possess large (hyper)polarizabilities and could bring a variety of linear and nonlinear optical properties. In the present work, we discuss the correlation between the atomic and electronic structures and the linear optical properties, investigated both theoretically and experimentally. In particular, we discuss the role of the HBs for the specific optical properties, in view of the electron density distribution, following our recent work.<sup>12</sup> This paper also reports on the determination of optimal positions for the hydrogen atoms, even in the absence of neutron diffraction data, and their implication on the electron density refinements.

## 2. EXPERIMENTAL SECTION

**2.1. Synthesis and Crystallization.** By interaction of L-histidine with oxalic acid, one could expect rather rich crystal chemistry. In fact, a systematic investigation allowed obtaining a number of unknown compounds on which we will report in a forthcoming paper. Species **1**, however, was previously reported by Prabu et al.,<sup>10</sup> who prepared crystals of L-histidinium hydrogen oxalate by slow diffusion of acetone into an aqueous solution. Instead, we obtained L-histidinium hydrogen oxalate by mixing aqueous solutions containing an equimolar amount of L-histidine (Sigma Aldrich, purity 99%) and oxalic acid (Fluka, purity 99%) at ambient temperature. Supersaturated solution was prepared and stirred thoroughly without any precipitate left. The solution was left for slow evaporation at ambient temperature; transparent crystals of large size and high purity were obtained after one day. The crystal habit was plate-like shape with *c* perpendicular to the plate (Figure 2). The synthesis was repeated several times to check the reproducibility of the crystals. It is interesting that using the racemic reagent D,L-histidine, instead of the enantiomerically pure L-histidine, we observed spontaneous resolution of a racemate of L-histidinium and D-histidinium hydrogen oxalates, with the same structure as **1**, but if crystals were grown from a solution stirred above 50 °C, an unprecedented racemate was observed, identified as a divalent salt of D- or L-histidinium oxalate ( $C_6H_{11}N_3O_2^{2+} \cdot C_2O_4^{2-}$ ), hereafter **2**. Further details of the complete crystal chemistry from histidine–oxalic acid mixture will be reported elsewhere.<sup>13</sup>

**2.2. Data Collection and Preliminary Refinements.** Suitable single crystals for X-ray diffraction analysis were carefully selected under a polarizing microscope and glued on a glass fiber. Single crystal X-ray diffraction experiment was performed on Agilent SuperNova (MoK $\alpha$  Al-filtered microsource<sup>14</sup>), equipped with an EoS detector, a motorized kappa goniometer along with Oxford Cryosystem 700 cryostream for low temperature. Two independent data collections were performed at 100 K and 110 K on two different samples. 110 K data collection was performed in  $\omega$  scan mode; a total of 2795 frames using a frame width of 1° were collected with an exposure of 10 s/30 s per frame, for 38 h. 100 K data collection was performed in  $\omega$  scan mode, a total of 3157 frames using a frame width of 1° were collected with an exposure of 12 s/40 s per frame, for 48 h. All the data were integrated using CrysalisPRO.<sup>15</sup> Analytical absorption correction was applied to the crystals, upon accurate indexing of the faces.

The quality of the crystals was good enough for full experimental determination of the electron density distribution,  $\rho(\mathbf{r})$ . The X-ray diffraction data were collected up to a resolution of 0.5 Å or better (0.45 Å for the data collection at 100 K). The coordinates of the known structure were used for initial least-squares refinements using SHELX97,<sup>16</sup> carried out to determine accurately positions and anisotropic thermal parameters for non-hydrogen atoms (using higher order data only). The crystal data and data collection details are given in Table 1. The final positional and equivalent isotropic thermal parameters of the non-hydrogen atoms are reported in Supporting Information.

**2.3. Multipole Refinement.** Multipolar refinements were carried out using the Hansen and Coppens formalism<sup>17</sup> implemented in the XD2006.<sup>18</sup>

**Table 1.** Crystal Data and Structure Refinement Parameters for L-Histidinium Oxalate

	L-histidinium hydrogen-oxalate	L- or D-histidinium oxalate
compound label	<b>1</b>	<b>2</b>
chemical formula	$C_6H_{10}N_3O_2^+ \cdot C_2O_4H^-$	$C_6H_{11}N_3O_2^{2+} \cdot C_2O_4^{2-}$
formula weight	245.2	245.2
crystal system	orthorhombic	orthorhombic
space group	$P2_12_12_1$	$P2_12_12_1$
Z	4	4
data set name	100 K	110 K
T/K	100	110
a/Å	5.5237(1)	5.5303(1)
b/Å	6.7090(2)	6.7229(1)
c/Å	26.8532(5)	26.8851(4)
V/Å <sup>3</sup>	995.14 (4)	999.58(3)
density (g/cm <sup>3</sup> )	1.62	1.63
<b>Data Collection</b>		
resolution (Å)	0.45	0.5
absorption $\mu$ (mm <sup>-1</sup> )	0.142	0.141
crystal dimensions (mm)	0.1 × 0.2 × 0.2	0.13 × 0.2 × 0.3
total reflections	58629	67298
unique reflections	11590	8431
$R_{int}$	0.0375	0.0405
$R_{\sigma}$	0.0273	0.0239
<b>Spherical Atom Refinement</b>		
$R_1$ ( $I > 2\sigma(I)$ )	0.0397	0.0373
$R_1$ (all data)	0.0431	0.0390
$wR_2$	0.1018	0.0961

$$\rho(\mathbf{r}) = \sum_{i=1}^{nat} \rho_i(\mathbf{r}) \quad (1)$$

$$\rho_{atom}(\mathbf{r}) = P_{core}\rho_{core}(\mathbf{r}) + P_{val}\kappa^3\rho_{val}(\kappa\mathbf{r}) + \sum_{l=0}^{l_{max}} \kappa'^3 R_l(\kappa'\mathbf{r})$$

$$\sum_{m=0}^l P_{lm\pm} Y_{lm\pm}(\Omega) \quad (2)$$

The electron density in the asymmetric unit is expanded in pseudoatomic contribution, and each of them is then split into  $\rho_c(\mathbf{r})$  and  $\rho_v(\mathbf{r})$  (core and valence electron densities), with the possibility to expand or contract the electronic shells (through the  $\kappa$  and  $\kappa'$  parameters), to deviate from neutrality (through the population  $P_{val}$ ; whereas  $P_{core}$  is kept frozen) or to distribute the density aspherically (through spherical harmonics,  $Y_{lm\pm}$  and relative populations  $P_{lm\pm}$ ). The radial part of the density functions is taken from atomic wave functions: the core and spherical valence functions are Volkov–Macchi ZORA atomic wave functions,<sup>18,19</sup> while the radial functions of the deformation part are simple Slater functions with energy-optimized exponents.<sup>20</sup> Each atom was assigned a finite multipole expansion, expanded at the octapolar level for C, N, and O and at the dipole level for H atoms (only dipole directed toward the X–H bond was included). A radial scaling for the spherical density was refined for each atom-type together with a scaling for the radial function for the deformation density ( $\kappa$  and  $\kappa'$  were constrained to be equal to avoid divergence).

It is known that non-centrosymmetric structures might produce bias in the multipolar expansion, due to the lack of information about the phase of each structure factor which is instead limited to 0 or  $\pi$  in the centrosymmetric case.<sup>21</sup> As it was demonstrated by Roversi,<sup>22</sup> the problem arises from “overparameterization” as some linear combinations of the odd-multipoles should be invariant, depending on the crystal class. In class 222, this is limited to one combination of octupolar

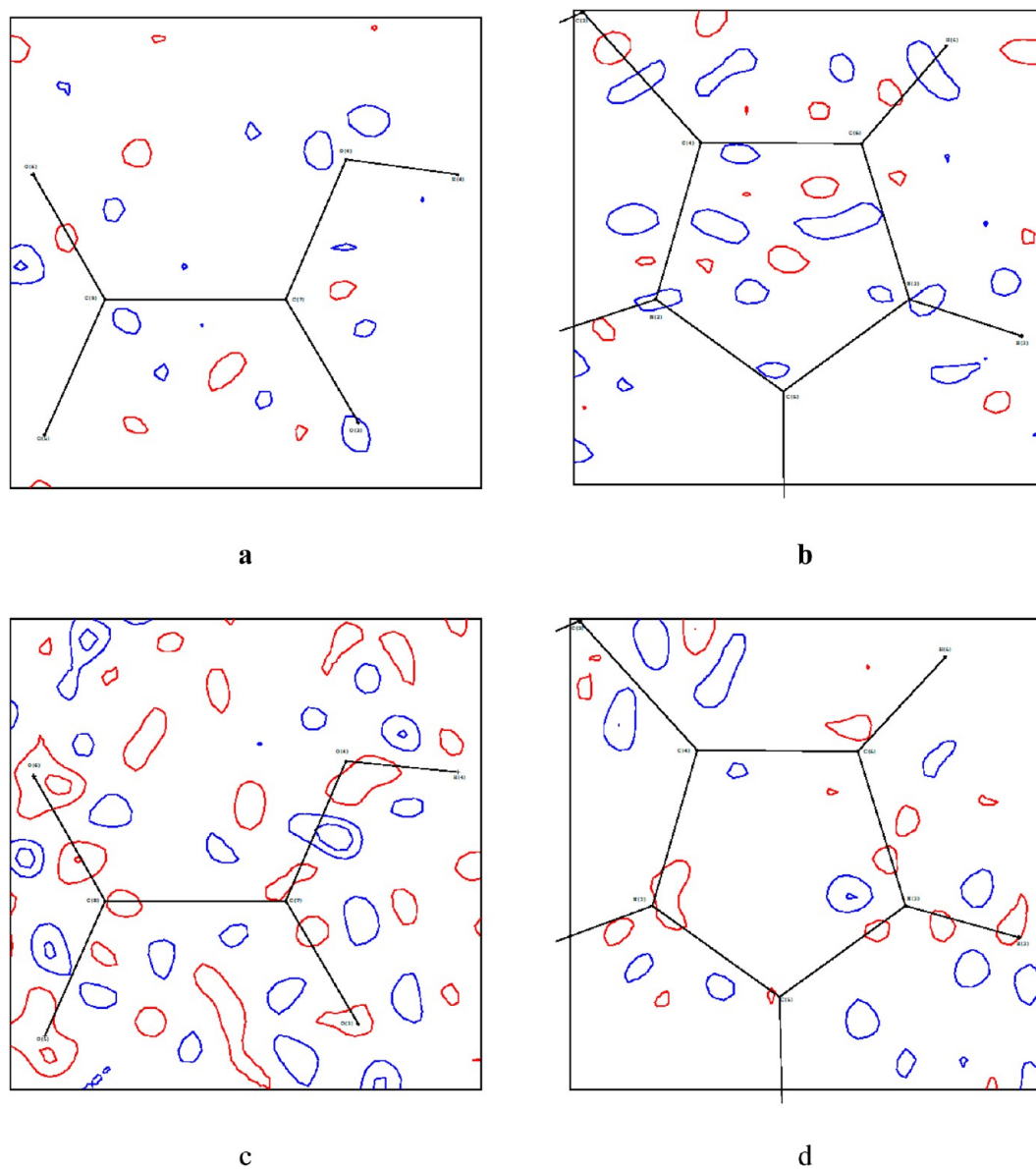


**Figure 1.** Residual density maps for the planes containing the hydrogen oxalate and the imidazole ring of L-histidinium for the 110 K data (a, b) and 100 K data (c, d) in charge constraint refinement conditions. Positive (blue) and negative (red) contour lines are drawn at a step width of  $0.1 \text{ e}/\text{\AA}^3$ . All the measured structure factors are used for these maps.

functions in the global framework of the cell, namely, the xyz octupole in the Cartesian form, or  $Y_{32}$ , using the spherical coordinate notation as in eq 2. Applying the appropriate constraint is difficult with XD2006 that adopts the local coordinate system approach, on the other hand very useful for exportability of the multipoles, instead of a global unit cell framework. It should be considered, however, that for the building block restrained refinements (see Discussion) the problem does not hold, because multipoles are constrained to values calculated theoretically for the ions in isolation. The rather close similarity of those results with the free unconstrained refinements guarantees that the problem has not affected these results. Moreover, as pointed out by Roversi,<sup>22</sup> the problem should be more consistent in smaller systems (fewer atoms per asymmetric unit) in higher non-centrosymmetric crystal class symmetries.

A Fourier peak search of the residual density resulted in peaks ranging from  $-0.21$  to  $0.26 \text{ e}/\text{\AA}^3$  for the 110 K data set and  $-0.29$  to  $0.31 \text{ e}/\text{\AA}^3$  for the 100 K data set in both refinements. These residuals are calculated from all the data with positive intensity collected up to a resolution of  $0.5 \text{ \AA}$  for both the data sets. The highest peak is located at  $0.7 \text{ \AA}$  from C(6) of imidazole ring of L-histidinium molecule (110 K data set),  $0.6 \text{ \AA}$  from

C(1) of carboxylic group of L-histidinium molecule (100 K data set). Residual density maps are shown in Figure 1. The observed residuals (based on all collected data) are low and without systematic features. For the 100 K data set, the residual density is more pronounced in the plane of the hydrogen oxalate, although this depends mainly on the higher resolution level which therefore includes a larger number of weaker reflections in the refinement and the Fourier summation.

Interestingly, the Meindl-Henn plots<sup>23</sup> and the normal distribution of residual density shows that the models are substantially unaffected from systematic effects; see Supporting Information.

**2.4. Theoretical Calculations.** Periodic density functional theory (PFT) calculations were performed using CRYSTAL09,<sup>24</sup> optimizing the crystal structure by minimizing the electronic energy of the unit cell, without including thermal energy and entropy, therefore at  $T = 0 \text{ K}$ . The functional adopted was B3LYP,<sup>25</sup> and the basis set was Pople-type 6-31G(2d,2p), which is one of the largest basis set that can be used in these kinds of calculations.

Optical properties of the periodic system were calculated on the optimized geometry using the couple perturbed Kohn–Sham theory; see Table 2. Using a rough approximation, the refractive index of a



Table 2. Refractive Indices along the Crystallographic

	experiment	PDFT (B3LYP)
<i>a</i>	1.63	1.58
<i>b</i>	1.50	1.45
<i>c</i>	1.60	1.63

molecular crystal could be derived from the first-order isotropic molecular polarizability through the Clausius–Mossotti equation.<sup>26</sup> However, the situation is quite more complicated: first of all molecules (or molecular ions as in this case) are in general quite anisotropic; moreover, there is a mutual interaction between molecules in aggregation, in part due to a short-range effect such as hydrogen bonding, in part due to long-range electrostatic interactions (induced polarization). In order to understand the effect of neighboring molecules on atomic and molecular polarizabilities of L-histidinium hydrogen oxalate, we have calculated polarizability tensors for the two ions in isolation as well as in the first coordination sphere of hydrogen bonded neighbors of the crystal structure. Thanks to the approach we have recently proposed,<sup>12</sup> we can calculate distributed atomic polarizabilities from gas phase single point calculations, using the experimental geometries of the 100 K model. Wave functions were calculated in the absence and in the presence of an applied electric field of magnitude 0.001 au at the B3LYP/6-311++G(2d,2p) level of theory, using Gaussian09.<sup>27</sup> The corresponding charge densities were partitioned in keeping with the ideas of QTAIM using the AIMAll package.<sup>28</sup> Atomic and molecular polarizability tensors were then calculated using PolaBer,<sup>12</sup> which performs numerical derivatives of the electric dipole moment with respect to the applied field. This allows reconstructing a more sensible molecular polarizability (i.e., of the molecule in the crystal environment) to be used for understanding the actual origin of the crystal linear susceptibility and therefore to justify the computed or observed refractive indices.

**2.5. Measurement of the Refractive Indices.** Refractive indices for the crystals of L-histidinium hydrogenoxalate were experimentally determined by the central illumination method (Becke line method).<sup>29</sup> This method is based on the observation of so-called Becke lines movement. The Becke bright halo lines are created near the junction between the crystal and the liquid as a result of refraction at the lens-like edge of the crystal. The lines are especially profound when there is a large difference of refractive indices between the two media. Becke lines movement can be observed when the image is thrown slightly out of focus. When the refractive index of crystal is near to that of the liquid, the crystal becomes almost transparent with Becke lines faint and usually colored. The observed colors (Becke line dispersion staining)<sup>30</sup> are the result of refractive index dispersion. Because the dispersion is typically lower for the crystal than for the liquid, it is not possible to get a match of refractive indices for all the wavelengths of light simultaneously. When the white light is used, the refractive index match is usually done for the yellow light ( $n_D$  where  $D = 589$  nm). At this point, the Becke line observation shows yellow-orange line moving into the crystal and a blue line moving into the liquid, as the stage of the microscope is lowered against the objective.

The accurate determination of refractive indices of the L-histidinium oxalate crystals (Figure 2) was done in the polarized light with the usage of Axio Scope.A1 microscope (Carl Zeiss Microimaging GmbH). Crystals were immersed in liquid of known refractive index on a glass slide under the coverslip. The prepared sample was then moved under the polarizing microscope and viewed through the 20 $\times$  objective. Several immersion liquids were tested to determine three refractive indices in different orientations of the crystal.

The matches for the three refractive indices of the examined crystals were done using a mixture of xylen isomers ( $n_D = 1.496$ ,  $T = 298$  K) and a mixture of bromoform ( $n_D = 1.598$ ,  $T = 298$  K) with methylene iodide ( $n_D = 1.742$ ,  $T = 298$  K). The usage of appropriate liquids allowed determination of the refractive indices of the crystals. Because of the natural crystal habit, it is very difficult to measure the  $n_c$  refractive index, and the value is an approximate one. The values of the refractive indices are present in Table 2. They are compared with theoretical values which

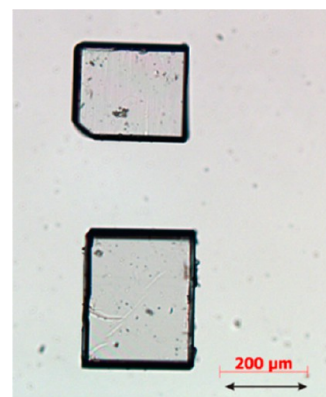


Figure 2. Crystals of 1 in two orientations against the vibration direction of plane polarized light marked with arrows.

are calculated using density functional theory and assuming no oscillation of the electric field (thus,  $\lambda = \infty$ ).

### 3. RESULTS AND DISCUSSION

The discussion is structured as it follows: first we analyze in detail the molecular and supramolecular structures; then we illustrate the theoretical breakdown of the crystal linear susceptibility in order to directly correlate the atomic and molecular polarizabilities with the crystal properties; finally, we analyze the features of the accurate electron density distribution (calculated or experimental) and empirially correlate them with the crystal properties.

**3.1. Crystal Structure Description.** The atomic numbering scheme of 1 is shown in Figure 3. The asymmetric unit contains

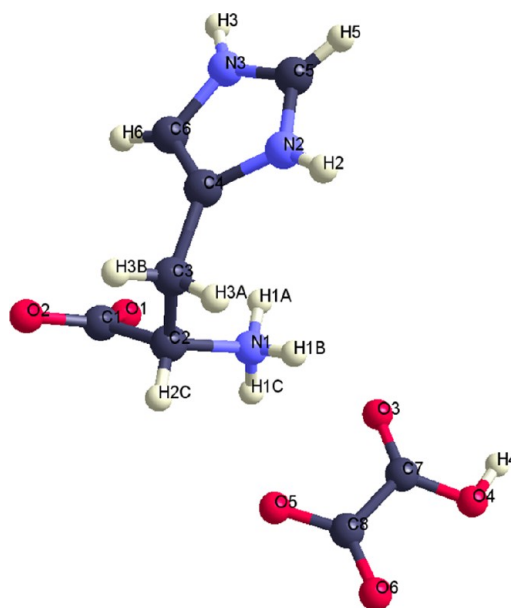
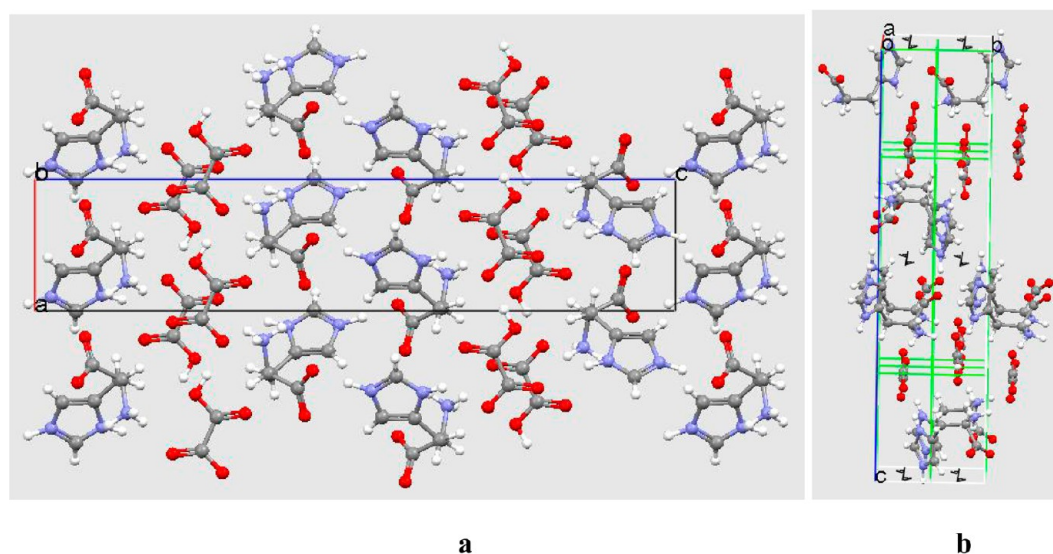


Figure 3. Atomic numbering scheme for L-histidinium hydrogenoxalate.

one L-histidinium and one hydrogen-oxalate. The solid state theoretical calculations and the experimental measures confirm that the oxalic acid is a semioxalate or hydrogen-oxalate monoanion and that the L-histidine is monocationic with protonated amino and imidazole groups and a negatively charged carboxylate group. As anticipated the ions aggregate into chains, that form alternating layers, stacked along the longest



**Figure 4.** (a) L-Histidine hydrogen-oxalate showing the alternating layers along the longest crystallographic axis (*c* axis); (b) histidine layer shown along *a*.

**Table 3.** Hydrogen Bonding Parameters in the L-Histidinium Hydrogen-Oxalate from the Charge-Constrained Model with Theoretical Position of H Atoms<sup>a</sup>

	donor–H...acceptor	D–H	H...A	D...A	D–H...A
N–H...O ammonium	N(1)–H(1A)...O(2) <sup>a</sup>	1.03	2.00	2.9280(6)	148
	N(1)–H(1B)...O(6) <sup>b</sup>	1.03	1.83	2.7982(7)	156
	N(1)–H(1C)...O(5) <sup>c</sup>	1.04	1.91	2.8915(7)	155
N–H...O imidazole	N(2)–H(2)...O(3) <sup>d</sup>	1.03	2.06	2.8681(6)	134
	N(2)–H(2)...O(5) <sup>d</sup>	1.03	2.10	2.9975(6)	145
	N(3)–H(3)...O(1) <sup>e</sup>	1.07	1.54	2.6089(7)	176
O–H...O hydrogen oxalate	O(4)–H(4)...O(5) <sup>a</sup>	1.04	1.47	2.5052(5)	175

<sup>a</sup>Distances are in Å, angles in °. Estimated standard deviations are given in parentheses (computed only for D...A). Symmetry operations to generate HB acceptor atoms: a:  $1 + x, y, z$ ; b:  $2 - x, 1/2 + y, 1/2 - z$ ; c:  $x, y, z$ ; d:  $x, 1 + y, z$ ; e:  $1/2 + x, 1/2 - y, -z$ .

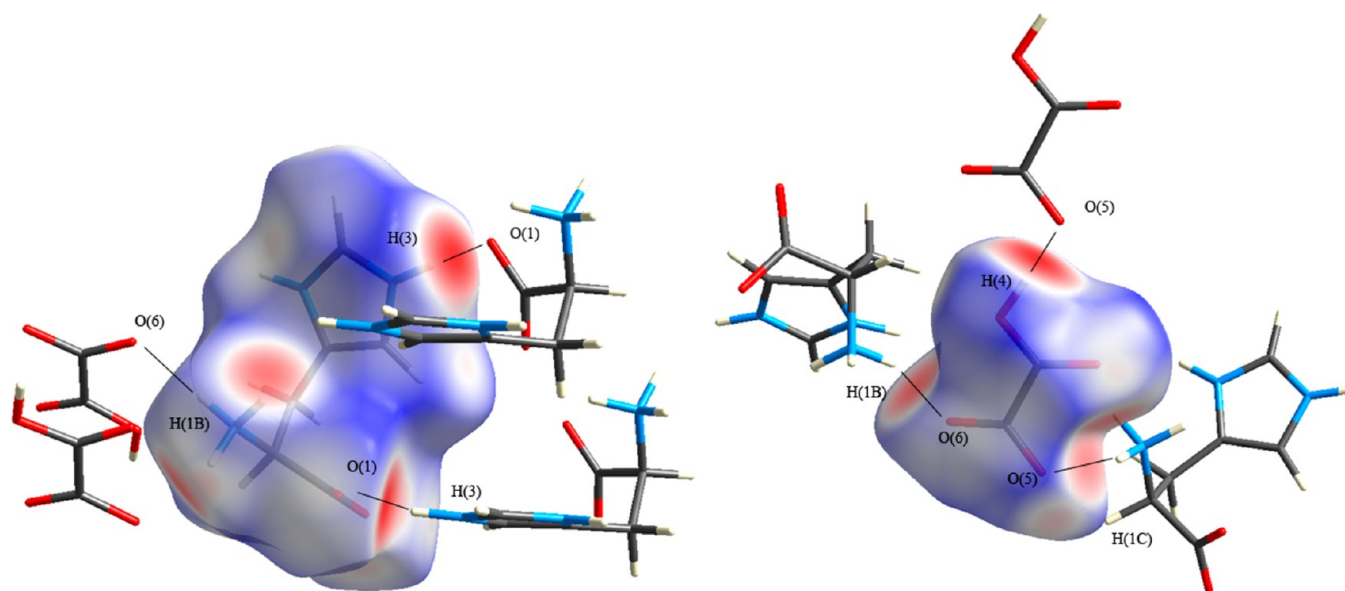


**Figure 5.** Left: Hirshfeld surface of L-histidinium in **1** with  $d_{\text{norm}}$  plotted from  $-0.83$  (red) to  $1.1$  (blue) Å (a negative value indicates a contact shorter than the sum of van der Waals radii). The volume inside the L-histidinium Hirshfeld surface is  $172 \text{ Å}^3$ . Right: Hirshfeld surface of hydrogen oxalate in **1** with  $d_{\text{norm}}$  plotted from  $-0.89$  (red) to  $0.73$  (blue) Å. The volume inside the hydrogen oxalate Hirshfeld surface is  $70 \text{ Å}^3$ .

crystallographic axis *c* (see Figure 4a). The L-histidinium layer is made of helical columns generated by the  $2_1$  screw axes parallel to

*a*, as shown in black in Figure 4b. The hydrogen-oxalate ions form chains parallel to *a* and stacked in layers along *b*.

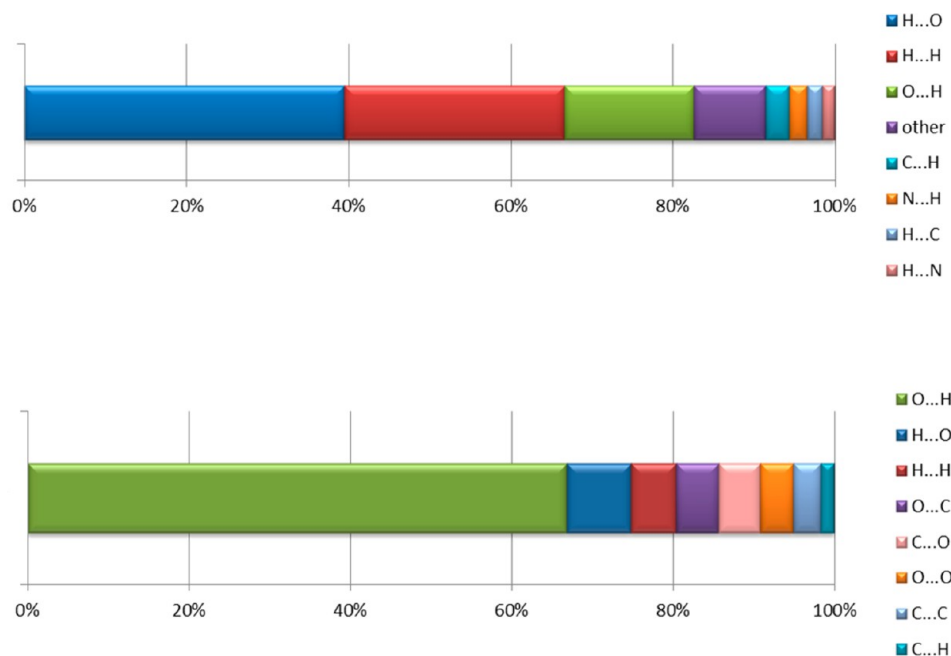


**Figure 6.** Breakdown of the close contacts on the Hirshfeld surfaces of the L-histidinium (top) and the hydrogen oxalate (bottom).

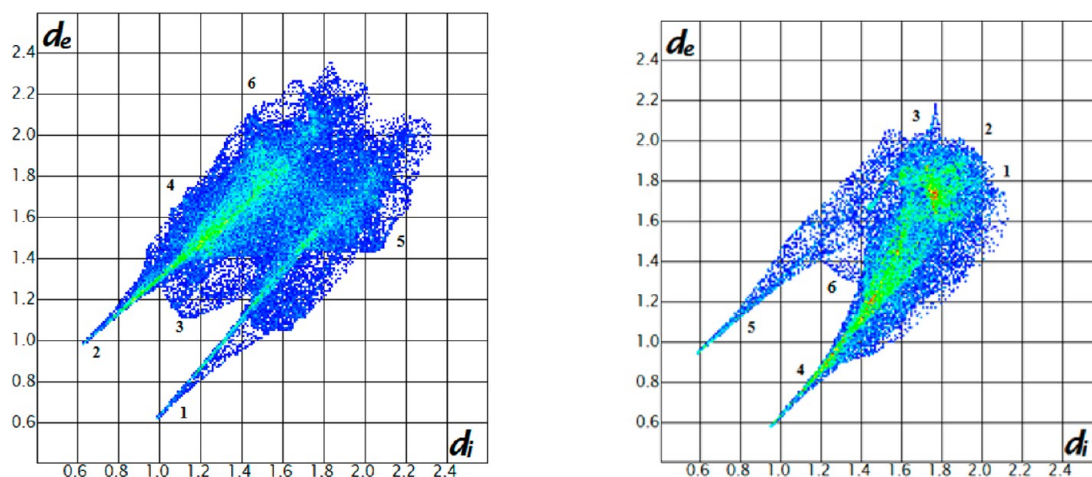


**Figure 7.** Left: Fingerprint plot of L-histidinium molecule in L-histidinium hydrogen oxalate. Close contacts: 1 is O $\cdots$ H, 2 is N $\cdots$ H, 3 is H $\cdots$ H, 4 is H $\cdots$ O, 5 is C $\cdots$ H, and 6 is H $\cdots$ C. Right: Fingerprint plot of hydrogen oxalate molecule in L-histidinium hydrogen oxalate. Close contacts: 1 is C $\cdots$ O, 2 is O $\cdots$ C, 3 is O $\cdots$ O, 4 is O $\cdots$ H, 5 is H $\cdots$ O and 6 is H $\cdots$ H.

One of the interesting features of **1** is that it possesses very short hydrogen bonds interconnecting the ions. In particular, the two strongest HBs are the interchain O–H $\cdots$ O $^-$  (2.5052(5) Å) that links hydrogen oxalates and the  $^+\text{N}$ –H $\cdots$ O $^-$  (2.6089(7) Å) that links imidazole and carboxylate groups of two L-histidinium; see Table 3. A medium-strong  $^+\text{N}$ –H $\cdots$ O $^-$  type hydrogen bond (2.7982(7) Å) is present between the ammonium group (NH $_3^+$ ) of the L-histidinium cation and one oxygen of the hydrogen oxalate. Weaker hydrogen bonds connect the hydrogen oxalate (acting as acceptor) and the ammonium or the imidazole groups of L-histidinium (donor).

**3.2. Visualization of Intermolecular Interactions through Hirshfeld Surfaces.** The Hirshfeld Surfaces (HS)<sup>31</sup> of the L-histidinium and the hydrogen oxalate ions in **1** have been generated, and the normalized contact distance  $d_{\text{norm}}$  were plotted on top of them, using CrystalExplorer<sup>32</sup> (Figure 5a,b). The HS analysis is interesting because it visualizes the *area of influence* of an intermolecular interaction. For example, the red

regions on the surfaces in Figure 5a,b highlight the hydrogen bond sites of the L-histidinium cation and the hydrogen oxalate anion, respectively. In fact, these regions address a very short contact with an atom inside the surface and a nearby ion (shown in the picture outside the surfaces).

This *area of influence* can be quantified by partitioning the HS in terms of the closest internal and external atoms, thus measuring the portion of a surface “belonging” to a given intermolecular contact (some examples are shown in the Supporting Information). From the histograms in Figure 6, we can visualize the relative contribution of each interaction type on L-histidinium and hydrogen oxalate. It is not surprising that the hydrogen bond is the dominating interaction in the entire structure (more than 50% for L-histidinium and more than 70% for hydrogen-oxalate), although other close contacts also play a role, including a large proportion of nondirectional H $\cdots$ H contacts between L-histidinium cations (27%), due to the side chain of the amino acid. Some H $\cdots$ H contacts also involve the



proton of the hydrogen oxalate, which is however largely dominated by O...H contacts (67%).

The intermolecular contacts can be represented also in the fingerprint scatter plots,<sup>33</sup> Figure 7, where  $d_i$  is the closest internal distance from a given point on the HS and  $d_e$  is the closest external contact. The fingerprint plot is divided into different regions based on the close contacts. The hydrogen bonding features in the closest environment of L-histidinium cation are labeled as 1 and 2, whereas for hydrogen oxalate anion as 4 and 5.

**3.3. Optical Indicatrix.** The refractive index measurement confirmed that the crystal is *biaxial* (i.e., it has two distinct optic axes as necessary for orthorhombic lattices) with a negative optic sign, Figure 8. In orthorhombic systems, the axes of the optical indicatrix and the crystallographic axes coincide.

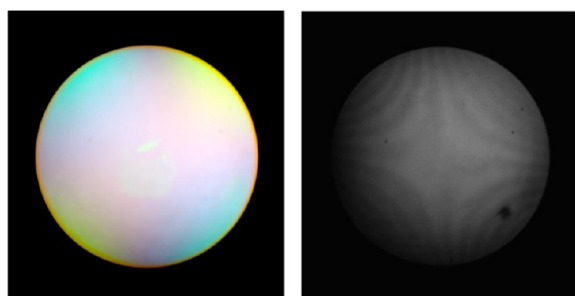


**Figure 8.** Left: reaction to the gypsum plate showing biaxial interference figure characteristic for the crystals of negative optical character.<sup>34</sup> Right: interference figure of the crystal plate oriented parallel to the optic axis plane.<sup>29</sup>

By comparing the crystal habit–structure relationship (see Figure 9) and the optical measures, it is concluded that the smallest refractive index coincides with  $b$  (see Table 2). The other two indices (along  $a$  and  $c$ ) are larger and more similar. The couple-perturbed Kohn–Sham calculations indicate a different order ( $n_c > n_a$ ) with respect to experiment. It should be considered that these calculations are carried out at zero frequency (i.e., without including oscillation of the applied

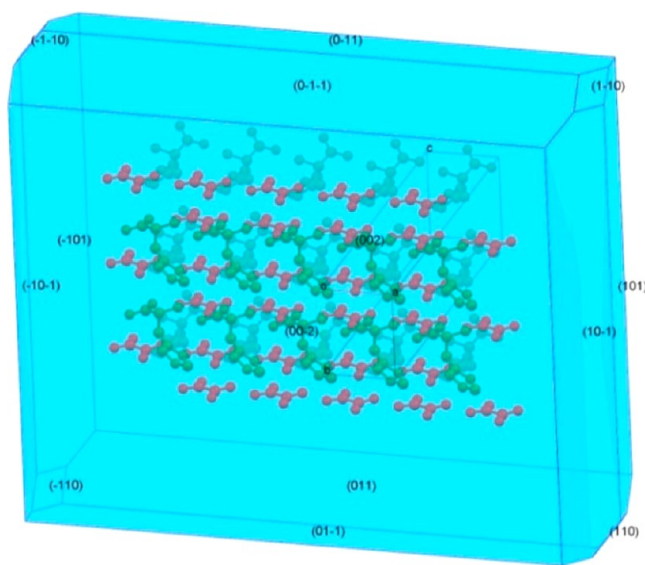


**Figure 9.** Crystal morphology of **1** in relation to the crystal structure. Hydrogen oxalate is red, and L-histidinium is green; hydrogen atoms are omitted for clarity.

electric field), and therefore they underestimate the refractive indices, measured instead at a finite frequency. In fact, theoretical  $n_a$  and  $n_b$  are 0.05 smaller than the experimental values, in keeping with many simulations. However, the theoretical  $n_c$  is apparently larger, but it is sensible to assume that the experimental determination is actually underestimated, probably because of the complicated measure along this direction, as anticipated in the Experimental Section.

The refractive indices provide important information on the intermolecular bonding in a crystal, because they depend on the interaction of photons with matter. The anisotropy of the optic indicatrix depends on the non-homogeneous way in which the ions are arranged in the structure and linked to each other; this is particularly cogent for the dominating intermolecular interactions, such as the hydrogen bonds. Indeed, this crystal is extremely birefringent ( $\Delta n_{\max} = 0.14$ , from experiment; 0.18 from theory): along the *fast* direction (smaller  $n$ ) there is a smaller resistance against the electric field of the incoming photons, which means there is less electron density to be polarized. The fastest direction is along  $b$ , i.e., perpendicular to the O–H...O<sup>−</sup> HB of the hydrogen oxalate chain (lying in the  $ac$  plane) and to the <sup>+</sup>N–H...O<sup>−</sup> of the L-histidinium helices (mainly elongated along  $c$ ). Instead, along  $b$  no strong HBs are active.

**3.4. Ion Polarizabilities and Correlation with the Optical Indicatrix.** Electric dipole (hyper)polarizabilities ( $\alpha$ ,  $\beta$ ,  $\gamma$ , ...) of atoms and molecules determine the electronic and optical responses of materials. For example, the refraction of light or the Raman scattering depend on the first-order dipole polarizability, the second-order tensor  $\alpha^{(2)}$  (measured in the unit of a volume). In a crystalline solid, the properties are regulated by the electric susceptibilities ( $\chi^{(1)}$ ,  $\chi^{(2)}$ ,  $\chi^{(3)}$ ), which could be considered as the periodic extension of the (hyper)polarizabilities, although susceptibilities are more precisely polarizabilities per unit of volume, therefore dimensionless.

In principle, in a molecular crystal, the electric susceptibilities could be obtained through summation of the molecular polarizabilities, taking into account mutual influence of all the molecules in a lattice within classical electrostatics (a local field effect).<sup>35</sup> However, one should take into account also the intermolecular electronic transitions that require proper quantum mechanical treatment. A simple oriented-gas model based on the additivity hypothesis is widely used for predicting the susceptibilities of molecular based materials. In this model, the perturbation of intermolecular interactions is neglected, and (hyper)polarizabilities are added up taking into account the molecular orientation.<sup>36</sup> Doubts were cast on the validity of this model,<sup>37</sup> and nowadays it is quite established that intermolecular interactions, especially hydrogen bonds, break the additive scheme at least when dealing with nonlinear susceptibilities ( $\chi^{(2)}$ ,  $\chi^{(3)}$ , ...).<sup>38</sup> On the other hand, the first-order polarizability  $\alpha$  is mainly due to intramolecular chemical bond effects rather than intermolecular interactions, and the additivity hypothesis is more valid.<sup>38</sup> Recent works showed the importance of local field corrections to match the experimental refractive index.<sup>39</sup>

Similarly to the charge distribution, one would prefer to analyze atomic  $\alpha_i$  rather than the molecular  $\alpha$ , especially because this allows appreciation of the role of each atom or functional group in a molecule. In this respect, there have been some proposals to calculate distributed atomic polarizabilities, i.e., to breakdown the total molecular polarizability into atomic contributions.<sup>40</sup> Recently, some of us developed a methodology to calculate and visualize atomic  $\alpha_i$  tensors, tested for many



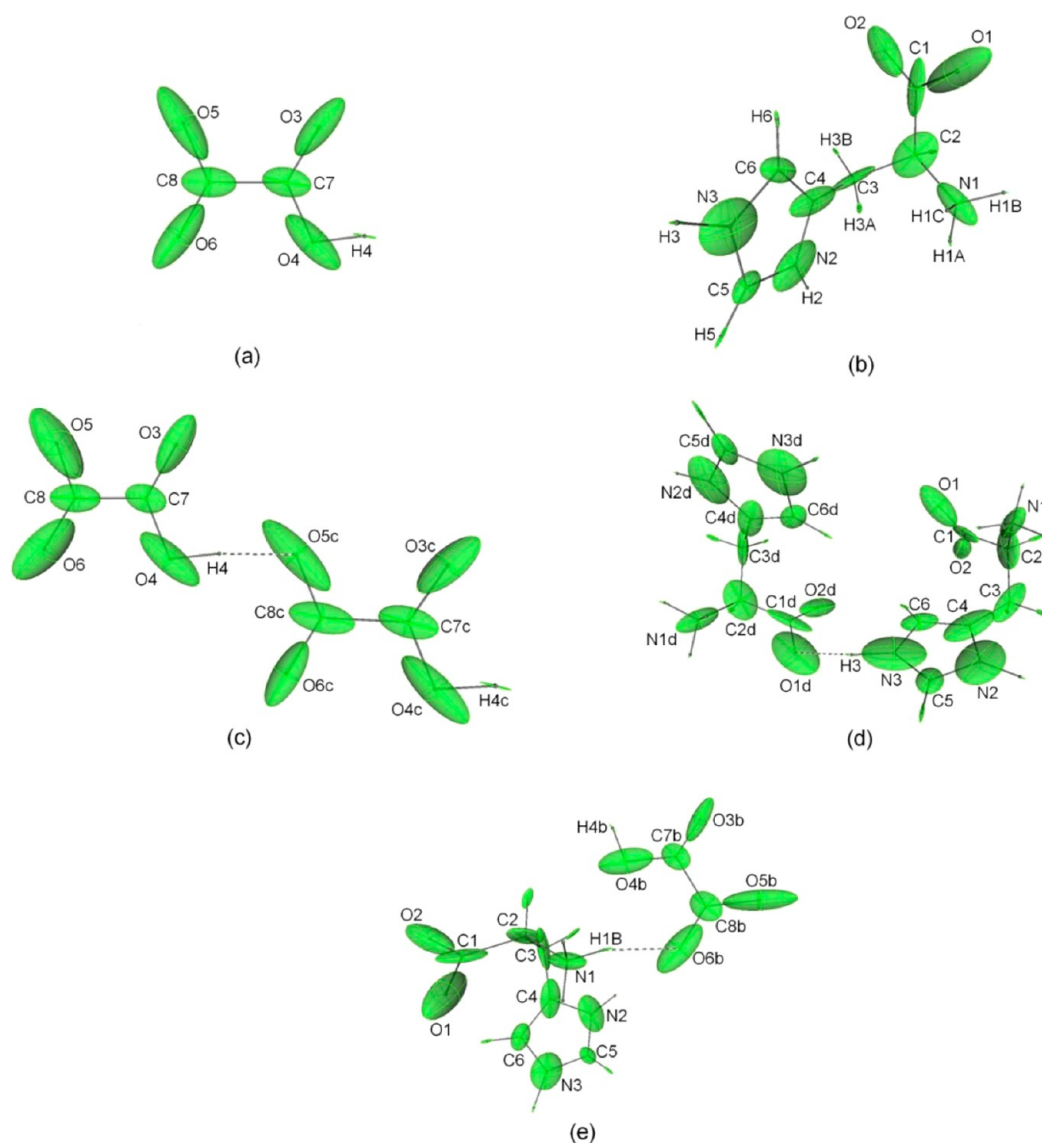


**Figure 10.** Atomic polarizability ellipsoids for (a) isolated hydrogen oxalate anion, (b) isolated L-histidinium cation, (c) hydrogen oxalate dimer bounded by O4–H4...O5 hydrogen bond, (d) L-histidinium dimer bounded by N3–H3...O1, and (e) L-histidinium hydrogen oxalate bounded by N1–H1B...O6. The scaling factor of polarizabilities is  $0.4 \text{ \AA}^{-2}$ .

compounds, including some amino acids.<sup>12</sup> The polarizability is calculated for each atom from the numerical derivation of the atomic dipole moment with respect to the electric field. This requires an atomic partitioning of the electron density, for example, using the QTAIM.<sup>41</sup> In order to avoid the well-known problems due to origin dependence, the method suggested by Keith<sup>42</sup> was adopted: the atomic dipole is partitioned into a polarization term (the dipole calculated inside an atomic domain) and a charge translation term (the dipole generated by distributing the atomic charges at bond critical point sites). Noteworthy, the method can be safely used also for non-neutral molecules, the additivity to a molecular polarizability is always perfect (if the electron density partitioning is exact), and the exportability is in general very good.<sup>12</sup> Within this approach, the atomic polarizability tensors are visualized as ellipsoids in the same three-dimensional real space as the molecule, assuming  $1 \text{ \AA}^3 \equiv 1 \text{ \AA}$ , although normally a scaling factor is necessary to reduce the size of polarizability ellipsoids for visualization purposes.

Here, we report the results of distributed atomic polarizabilities calculated for the ions of species **1**, focusing on the intra- and intermolecular factors which mainly affect the  $\alpha$ 's; see Figure 10. In general, the atomic polarizabilities are larger along the bond directions, especially toward atoms with high polarizabilities and connected through stronger bonds. This is a simple "cooperative" effect that could be justified also with classical electrostatics, but it can be calculated with precision only using proper quantum mechanical treatment. In fact, the polarizability ellipsoids of oxygen atoms are elongated along the C–O bonds in the carboxylate or carboxylic groups. For hydroxyl oxygens, however, there is a small rotation due to the O–H bond. H has a very small polarizability (prolated along the X–H bond direction) due to its low electron population, and therefore it has only a minimal influence on its neighbors. The  $sp^2$  hybridized carbon atoms are normally associated with oblate ellipsoids, to better account for their trigonal coordination. In the imidazole ring, atomic polarizabilities are spread over the plane of the ring: N(2) and N(3) are more polarizable than the C atoms, as expected.

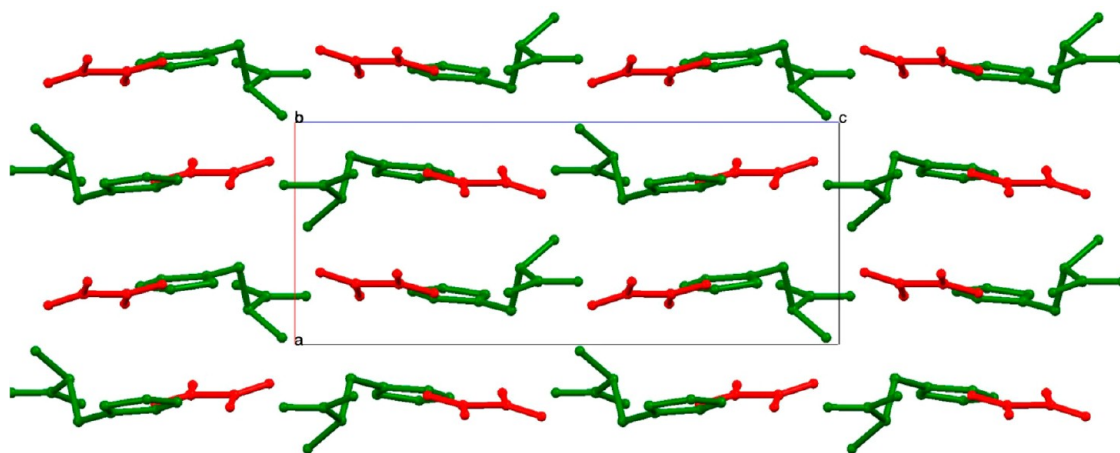


**Figure 11.** The crystal packing of  $\text{C}_6\text{H}_{11}\text{N}_3\text{O}_2^{2+} \cdot \text{C}_2\text{O}_4^{2-}$  (**2**). Histidinium is plotted in green and oxalate is in red. At variance from **1**, this structure is not characterized by homoionic chains or helices.

With our approach, it is possible to analyze the behavior of the two ions in aggregation, by calculating the atomic polarizabilities in all the dimers produced by the stronger HBs of **1** (see Figure 10c–e). From Figure 10c, we see that O5c (the HB acceptor in a hydrogen oxalate dimer) slightly modifies the orientation and stretching of its polarizability tensor, due to the hydrogen bond. In general, the whole anion changes the shape of the polarizability tensor, which becomes larger in the HB direction. However, the isotropic polarizability (calculated as the arithmetical average of the diagonal tensor components) does not change significantly. For example, in a hydrogen oxalate dimer, the two anions have  $\alpha_{\text{iso}} = 49.4$  (HB donor) and 48.8 Bohr<sup>3</sup> (HB acceptor), whereas for the isolated hydrogen oxalate  $\alpha_{\text{iso}} = 48.3$  Bohr<sup>3</sup>. On the contrary, the anisotropy of the tensor is much more affected:  $\alpha_{11}/\alpha_{33}$  (the ratio between the largest and smallest components) is 2.05 for an isolated anion but 2.45 for the HB acceptor anion in a dimer and 2.40 for the central anion of a trimer (acting both as acceptor and donor, not shown in the figure). This means that the hydrogen oxalate chain motif in **1** should produce a larger crystal polarizability (hence susceptibility) along the direction of the chain (*a*) for two reasons: (a) the chains elongate along the direction of larger component of the anion polarizability; (b) the HB increases by ca. 20% the anisotropy of the polarizability in the same direction. The second important direction is *c* because the molecular plane of all hydrogen oxalates is in fact parallel to *ac* (thus, many C=O bonds have components also along *c*). In fact, a hypothetical breakdown of the crystal susceptibility shows that the hydrogen oxalate anions would give a large anisotropy.  $\chi_{11} = 0.45$ ,  $\chi_{22} = 0.22$ , and  $\chi_{33} = 0.41$  are calculated after summation of the polarizabilities of the four gas phase anions as oriented in the unit cell. This is further increased if we use the polarizabilities of hydrogen oxalates computed for the anion embedded in a chain ( $\chi_{11} = 0.50$ ,  $\chi_{22} = 0.21$ , and  $\chi_{33} = 0.37$ ).

On the other hand, the L-histidinium is itself more isotropic ( $\alpha_{11}/\alpha_{33} = 1.36$  in isolation) than hydrogen oxalate. Moreover, it is not oriented to maximize the polarizability along any specific crystallographic direction. Therefore, the contribution to the crystal susceptibility is overall rather isotropic ( $\chi_{11} = 0.70$ ,  $\chi_{22} = 0.64$ , and  $\chi_{33} = 0.67$  using the polarizabilities calculated for the isolated cation and summing up the four cations in the cell). The isotropic molecular polarizability of L-histidinium is not much affected by the hydrogen bond (Figure 10d):  $\alpha_{\text{iso}} = 92.6$  and 86.5 Bohr<sup>3</sup>, for the hydrogen bond donor and acceptor molecules,

compared to  $\alpha_{\text{iso}} = 89.8$  Bohr<sup>3</sup> for the isolated cation. However, the strong HB that connects the two cations is highly directional (almost parallel to *c*). If we calculate the contribution to crystal susceptibility using a cation perturbed by two other cations in the L-histidinium helices, then  $\chi_{33}$  would be quite enhanced ( $\chi_{11} = 0.67$ ,  $\chi_{22} = 0.61$ , and  $\chi_{33} = 0.79$ ).

The combined effects of L-histidinium and hydrogen oxalate produce the larger  $\chi_{11}$  and  $\chi_{33}$  components ( $\chi_{11} = 1.17$ ,  $\chi_{22} = 0.82$ , and  $\chi_{33} = 1.16$ , from which one would calculate  $n_a = 1.47$ ,  $n_b = 1.35$ ,  $n_c = 1.47$ ). If we then consider the Lorentz correction for the lattice effects on the local field<sup>34</sup> (i.e., increased polarizability due to induced electric moments of all molecules in the crystal), the refractive indices become  $n_a = 1.62$ ,  $n_b = 1.43$ ,  $n_c = 1.61$ , which are quite close to those calculated *ab initio* from couple-perturbed Kohn–Sham theory (see Table 2), although  $n_a$  results are larger, as from the experiment determination. The perturbation of the crystal packing on the isolated anions is also evident from the enhancement of the molecular dipole moments, a feature typically observed in crystals, although the extent is often debated.<sup>43</sup> Here this comparison is a bit problematic because, talking about ions, the two dipole moments would be origin dependent. Anyway, based on the multipolar refinements described in the next section and using the center of mass as reference (for the geometries of the ions as in the crystal), an enhancement is observed for both ions: from 4.4 to 6.1 D for hydrogenoxalate and from 13.3 to 15.5 D for L-histidinium. This is in agreement with an enhancement of the two polarizabilities as well.

Further adjustment of the molecular polarizabilities are possible taking into account also the HB between the cation and the anion (Figure 10e), which are however weaker than the two homoionic ones. The molecular  $\alpha_{\text{iso}}$  for the hydrogen oxalate (HB acceptor) is 45.8 Bohr<sup>3</sup>, i.e., smaller than the isolated anion, whereas  $\alpha_{\text{iso}}$  for L-histidinium (93.5 Bohr<sup>3</sup>) is larger than in isolation, in keeping with a small charge transfer from the anion to the cation. The anisotropy of the hydrogen oxalate is also increased by this interaction ( $\alpha_{11}/\alpha_{33} = 2.57$ ), which reduces the polarizability component along the direction perpendicular to the main plane of the molecule (i.e., in the direction of the *b* axis).

With this analysis, we can conclude that the measured or calculated crystal refractive indices reflect mainly the specific orientation of the molecular polarizabilities of the ions, especially of the hydrogen oxalates. The perturbation of the HBs is not large, but anyway contributes to stretch the polarizability tensors

**Table 4.** XD Refinements with Different Positioning of Hydrogen Atoms (Based on all Data with  $I > 0$ ). Shaded Cells Indicate the Problem of  $U_{\text{iso}}$  for One or More Hydrogen Atoms

H positions	100K ( $d_{\text{min}} = 0.45 \text{ \AA}$ )				100K (truncated at $d_{\text{min}} = 0.5 \text{ \AA}$ )				110K ( $d_{\text{min}} = 0.5 \text{ \AA}$ )			
	Charge Constraint $U_{\text{iso}} < 0$		Charge Transfer $U_{\text{iso}} < 0$		Charge Constraint $U_{\text{iso}} < 0$		Charge Transfer $U_{\text{iso}} < 0$		Charge Constraint $U_{\text{iso}} < 0$		Charge Transfer $U_{\text{iso}} < 0$	
	$R(\text{F})$		$R(\text{F})$		$R(\text{F})$		$R(\text{F})$		$R(\text{F})$		$R(\text{F})$	
Neutron averages <sup>(a)</sup>	0.0341		0.0341		0.0277	H(3) H(4)	0.0277		H(1B) H(3)	0.0279		0.0272
NMR <sup>(b)</sup>	0.0341		0.0341		0.0277	H(3) H(4)	0.277		H(1B) H(3)	0.0279		0.0272
Refined X-H <sup>(c)</sup>	H(4)	0.0338	H(4)	0.0338	H(4)	0.0273	H(3) H(4)	0.0273		0.0270		0.0269
PDFT <sup>(d)</sup>		0.0341		0.0341		0.0278	H(3)	0.0277	H(1B) H(3)	0.0280		0.0273
PDFT+SHADE <sup>(e)</sup>		0.0343		0.0343		0.0279		0.0279		0.0283		0.0274
Theoretical multipoles+neutron averages <sup>(f)</sup>		0.0382				0.0323				0.0326		

<sup>a</sup>Frozen X–H distances from average neutron data for histidinium<sup>48</sup> and for hydrogen oxalate.<sup>49</sup> <sup>b</sup>Frozen X–H distances from NMR data<sup>45</sup> for histidinium and from neutron data<sup>49</sup> for hydrogen oxalate. <sup>c</sup>X–H distances freely refined. <sup>d</sup>Frozen X–H distances from periodic density functional calculations. <sup>e</sup>X–H distances as in d; ADPs of hydrogens calculated with SHADE.<sup>46</sup> <sup>f</sup>X–H distances as in model a; multipoles rigidly taken from theoretical calculations of the two isolated ions (building block approach).

in the *ac* plane. Both features, molecular and intermolecular, are in keeping with larger  $n_a$  and  $n_c$  and smaller  $n_b$  refractive indices (see Table 2) and therefore with the significant birefringence of 1.

An interesting comparison is possible with species 2, the unprecedented polymorphic form of histidinium oxalate. Although it was not possible to measure more accurate data and the refractive indices, Kohn–Sham calculations predict an even higher birefringence in that species,  $\Delta n = 0.19$ . 2 and 1 have the same orthorhombic  $P2_12_12_1$  space group, but the packing of 2 is completely different with dianionic oxalates surrounded only by histidinium dications (Figure 11). In this case, the oxalate anion, the carboxylic, and the imidazole group of histidinium (i.e., the three sources of polarizability) define planes which are almost parallel whose normal direction is almost parallel to *a*, which is therefore associated with a much smaller refractive index. An additional feature is favoring a large anisotropy: the high polarizability of a dianion such as oxalate, compared to hydrogen oxalate monoanion. Further study on this material and the complete crystal chemistry of histidine oxalate salts are in due course and will be reported in another paper.<sup>13</sup>

### 3. 5. Electron Density Modeling. 3.5.1. General Features.

The accurate electron density distribution of D,L-histidine from X-ray diffraction was reported by Coppens et al.<sup>44</sup> It crystallizes, of course, in zwitterionic configuration with molecules packed in layers and linked head to tail through strong imidazole–carboxylate and ammonium–imidazole hydrogen bonds. The electron density of L-histidine instead has not been investigated experimentally, so far.

The L-histidinium hydrogen oxalate is a crystalline salt which offers flexibility of the molecular design as discussed earlier. The concept of *building blocks* can be tested for the molecular cation and anion (although they are not the same building blocks of the M-BioMOFs materials we will investigate): their electron densities can be calculated in isolation and expanded in atomic distributed multipoles, following the Hansen and Coppens model<sup>17</sup> and checking how this model is different from a refinement of the relaxed molecular densities (i.e., mutually perturbed and exchanging electrons). Thus, several electron density refinements were tested against the measured X-ray

diffraction data: (1) *building block* model: electron density multipoles are rigidly imported from theoretical calculations of the two ions in isolation; (2) *charge constrained* model: the two ions are forced to +1 and –1 charge, although allowed to mutually polarize their electron densities; (3) *charge transfer* model, where both mutual induction and charge transfer are allowed. A summary of the refinement results are presented in Table 4.

Crucial parameters for each model are the positions of H atoms, which were constrained to meaningful X–H distances for each refinement; see Table 4 (Neutron diffraction beamtime was requested for this compound, but it was not awarded, so we cannot use accurate positioning of the H atoms.) Average neutron diffraction values were taken from the refinements of similar species in similar hydrogen bonding networks. Solid state NMR data are also available for 1.<sup>45</sup> A model using the X–H distances of the geometry optimization using PDFT calculations on 1 was also tested as well as a free refinement of H positions, a procedure that however may lead to unreasonable results. Apart from electron density parameters of H, the choice affects also the refined atomic displacement parameters. An alternative model was also tested: the anisotropic parameters for H atoms were calculated using the rigid body approximation of each ion and including internal motion from experimental X–H stretching using the software SHADE<sup>46</sup> and then keeping these parameters rigid during the refinement. This treatment is somewhat similar to the refinement proposed by Koritsanszky et al.<sup>47</sup> for potassium hydrogen-tartrate. From the Table 4, it can be observed that the refined  $U_{\text{iso}}$  of hydrogens are sometime problematic (negative or anyway quite close to 0). Models with X–H distances reset to theoretically predicted values reduce these problems in most cases. Otherwise, the SHADE model is an excellent alternative because it avoids  $U_{\text{iso}}$  refinement. Upon comparison of data set at the same resolution level, the close similarity between all the agreement indices of various models confirms that the X-ray data are not able to address one model as better. Therefore, the model constructed with theoretical X–H distance and  $U_{ij}$  from SHADE could be evaluated as the most accurate (although having slightly higher *R*-factors) because using less parameters in the refinement (thus reducing the correlation) and more information from

**Table 5. Charges of L-Histidinium (Hist) and Hydrogen Oxalate (Oxal) Ions from QTAIM or from Monopole Coefficients of the Charge Transfer Multipole Expansion for Different Models of H Positioning<sup>a</sup>**

H position	model											
	100 K ( $d_{\min} = 0.45 \text{ \AA}$ )				100 K ( $d_{\min} = 0.50 \text{ \AA}$ )				110 K ( $d_{\min} = 0.50 \text{ \AA}$ )			
	QTAIM		Multipole		QTAIM		Multipole		QTAIM		Multipole	
	hist	oxal	hist	oxal	hist	oxal	hist	oxal	hist	oxal	hist	oxal
neutron average	0.86	−0.82	0.82	−0.83	0.87	−0.84	0.84	−0.84	0.72	−0.71	0.68	−0.68
NMR	0.86	−0.83	0.83	−0.83	0.87	−0.84	0.84	−0.84	0.72	−0.71	0.69	−0.69
X–H refinement	0.78	−0.76	0.76	−0.76	0.79	−0.77	0.77	−0.77	0.66	−0.64	0.62	−0.62
theoretical	0.85	−0.83	0.83	−0.83	0.86	−0.84	0.84	−0.84	0.71	−0.70	0.68	−0.68
theoretical +SHADE	0.83	−0.80	0.82	−0.82	0.84	−0.81	0.82	−0.82	0.69	−0.67	0.66	−0.66

<sup>a</sup>The slight difference between absolute QTAIM charges is due to precision of the numerical integration within atomic basins.

external source. On the other hand, the model with X–H from neutron averages would be the most straightforward because it requests the least additional information, which is easily available from databases. It is interesting that all these models for H positions (apart from the free X–H refinement) reproduce a very similar electron density distribution, within the experimental error, as also evident from the calculation of the properties.

Another interesting comparison is that between the various constraints on the ion charges. The agreement indices of a *charge constrained* or a *charge transfer* model are very similar for the 100 K data set (whereas for the 110 K data set they are more dissimilar). This means that in general it cannot be easily assessed whether a charge transfer from the anion to the cation occurs or not and even minor differences in the data correction procedures might easily affect this value. On the other hand, using rigid *building blocks* a significant deviation is observed, which implies that apart from charge transfer the mutual perturbation of the ions is, at least in this strongly bonded salt, quite significant and well observable.

**3.5.2. Charges of the Ions in the Crystal.** The charges calculated from the quantum theory of atoms in molecules (QTAIM<sup>41</sup>) or from monopole coefficients of the multipolar expansion are reported in Tables 5 and 6, for all the investigated models. There is a clear dependence on the data set: for example, the 110 K data predict larger charge transfer between the ions (L-histidinium is less positive and hydrogen oxalate is less negative

than their formal +1 and −1). From the 100 K data, we learn that the resolution is only marginally relevant, as charges calculated from  $d_{\min} = 0.45 \text{ \AA}$  or  $d_{\min} = 0.5 \text{ \AA}$  models are very similar.

If the H atoms are fixed using external information (neutron diffraction, NMR, PDFT), the charges are quite similar, whereas if they are freely refined the molecular charges decrease. Albeit the agreement indices are slightly smaller, the refinement of H positions is not recommended, given the high correlation among the parameters (dipole functions and coordinates), which in this case produces significantly shorter, and unrealistic, X–H distances.

The QTAIM charges of the constrained models adhere to +1 and −1, in keeping with the fact that they normally mimic the sum of atomic monopoles (but not true for each individual atomic charge). The most interesting data are the QTAIM charge from the direct integration of the PDFT electron density, which gives  $\pm 0.85$  for the two ions. If this density is expanded in multipoles, using eq 2, we note that the computed charges are higher in absolute value, even if a flexible *charge transfer* model is refined. This means that the close similarity between QTAIM charges from the *charge transfer* 100 K multipolar model and from the direct integration of PDFT density is likely just incidental. The fluctuation observed in the various models refined from experimental data is an indication of the “actual” experimental uncertainty. We may conclude that even in the presence of strong hydrogen bonding, the least biased (and therefore more exportable) multipolar model is the *charge constrained* where ions are rigidly treated, in keeping with the discussion in the previous paragraph.

**3.5.3. QTAIM Analysis of Hydrogen Bonding.** A full QTAIM analysis was carried out on all experimental and theoretical electron density models of 1. The properties at the bond critical points of the most relevant HBs are listed in Table 7. All models are qualitatively in agreement: when comparing with PDFT calculations, we must consider that the optimized geometry is associated with shorter HBs, mainly due to neglecting the zero point vibration effects. Therefore, the theoretical density predicts in general stronger interactions, with the only exception of H(2)⋯O(5), which is predicted longer. The substantial equivalence between a charge constrained or a charge transfer refinement tells us that there is no special improvement from a more flexible model. It is interesting that the two stronger HBs, O(4)–H(4)⋯O(5) (interconnecting two hydrogen oxalates) and N(3)–H(3)⋯O(1) (interconnecting two L-histidinium cations) are associated not only with the larger electron density but also with a negative energy density, especially in the theoretical PDFT results, which is a clear sign of incipient covalency of the bonds.<sup>50</sup> Noteworthy, the vectors interconnect-

**Table 6. QTAIM or Multipole Charges of L-Histidinium and Hydrogen Oxalate Ions from Charge Constraint Model Using Theoretically Predicted H Position<sup>a</sup>**

model		QTAIM		Multipole	
		hist	oxal	hist	oxal
experimental data set charge constrained model	100 K ( $d_{\min} = 0.45 \text{ \AA}$ )	1.02	−0.99	1.00	−1.00
	100 K ( $d_{\min} = 0.50 \text{ \AA}$ )	1.02	−1.00	1.00	−1.00
	110 K ( $d_{\min} = 0.50 \text{ \AA}$ )	1.04	−1.02	1.00	−1.00
periodic DFT calculations	primary density	0.85	−0.85		
	charge constrained model	1.03	−1.00	1.00	−1.00
	charge transfer model	0.97	−0.94	0.93	−0.94

<sup>a</sup>For sake of comparison, the periodic B3LYP charges from primary density or from multipolar fitting are also given.



Table 7. Topological Analysis of Intermolecular Interactions at Bond Critical Points (bcp)<sup>a</sup>

interaction	model	data set	$\rho(r)$	$\nabla^2\rho(r)$	$R_{1-2}$	$d_1$	$d_2$	$\epsilon$	$G$	$H$
H(1A)⋯O(2) <sup>b</sup>	CC	100 K	0.130	1.87	2.02	0.73	1.29	0.02	0.11	0.02
	CC	110 K	0.106	1.95	2.04	0.75	1.30	0.18	0.11	0.03
	CT	100 K	0.129	1.97	2.02	0.74	1.28	0.05	0.12	0.02
	CT	110 K	0.105	1.95	2.05	0.75	1.30	0.20	0.11	0.03
	PDFT opt geom		0.155	1.73	2.03	0.77	1.26	0.03	0.12	0.00
H(1B)⋯O(6) <sup>c</sup>	CC	100 K	0.181	2.70	1.82	0.64	1.19	0.09	0.17	0.02
	CC	110 K	0.156	3.15	1.84	0.64	1.21	0.13	0.18	0.04
	CT	100 K	0.187	3.01	1.83	0.63	1.19	0.06	0.19	0.02
	CT	110 K	0.153	3.16	1.85	0.64	1.21	0.13	0.18	0.04
	PDFT opt geom		0.229	2.41	1.87	0.68	1.19	0.05	0.18	−0.01
H(1C)⋯O(5) <sup>d</sup>	CC	100 K	0.159	2.26	1.93	0.67	1.26	0.04	0.14	0.02
	CC	110 K	0.129	2.47	1.95	0.68	1.27	0.12	0.14	0.03
	CT	100 K	0.154	2.37	1.93	0.68	1.25	0.03	0.15	0.02
	CT	110 K	0.126	2.46	1.92	0.69	1.27	0.14	0.14	0.03
	PDFT opt geom		0.263	2.80	1.80	0.64	1.16	0.01	0.22	−0.02
H(2)⋯O(3) <sup>e</sup>	CC	100 K	0.159	1.98	2.09	0.84	1.25	0.11	0.13	0.01
	CC	110 K	0.111	1.66	2.11	0.80	1.31	0.08	0.10	0.02
	CT	100 K	0.124	1.70	2.12	0.82	1.30	0.07	0.10	0.01
	CT	110 K	0.117	1.72	2.09	0.80	1.30	0.04	0.10	0.02
	PDFT opt geom		0.229	2.43	1.86	0.67	1.19	0.02	0.18	−0.01
H(2)⋯O(5) <sup>e</sup>	CC	100 K	0.155	1.94	2.09	0.82	1.27	0.05	0.13	0.01
	CC	110 K	0.091	1.53	2.14	0.78	1.35	0.08	0.09	0.02
	CT	100 K	0.112	1.66	2.10	0.78	1.32	0.04	0.10	0.02
	CT	110 K	0.098	1.60	2.12	0.79	1.34	0.03	0.09	0.02
	PDFT opt geom		0.081	1.01	2.35	0.97	1.39	0.07	0.06	0.01
H(3)⋯O(1) <sup>f</sup>	CC	100 K	0.340	4.17	1.55	0.45	1.09	0.03	0.33	−0.04
	CC	110 K	0.325	4.56	1.54	0.46	1.08	0.04	0.34	−0.02
	CT	100 K	0.391	4.70	1.55	0.48	1.07	0.04	0.39	−0.06
	CT	110 K	0.349	4.33	1.54	0.47	1.07	0.04	0.34	−0.04
	PDFT opt geom		0.466	3.90	1.57	0.51	1.06	0.03	0.41	−0.13
H(4)⋯O(5) <sup>b</sup>	CC	100 K	0.508	5.38	1.47	0.45	1.02	0.02	0.51	−0.13
	CC	110 K	0.422	5.17	1.47	0.41	1.06	0.01	0.43	−0.07
	CT	100 K	0.439	6.12	1.47	0.44	1.03	0.03	0.49	−0.06
	CT	110 K	0.426	5.12	1.47	0.41	1.05	0.01	0.43	−0.07
	PDFT opt geom		0.560	3.69	1.49	0.46	1.03	0.02	0.48	−0.22

<sup>a</sup> $\rho(r)$  is given in  $\text{e} \text{Å}^{-3}$ ,  $\nabla^2\rho(r)$  in  $\text{e} \text{Å}^{-5}$ .  $d_1$  and  $d_2$  are distances between bcp and atom 1, 2 (Å),  $R_{1-2}$  is their summation.  $\epsilon$  ellipticity (dimensionless);  $G$  and  $H$  are the kinetic and total energy densities (in hartree  $\text{Å}^{-3}$ ). CC is a charge constrained model, and CT is a charge transfer model.

<sup>b</sup>Symmetry: 1 +  $x$ ,  $y$ ,  $z$ . <sup>c</sup>2 −  $x$ , 1/2 +  $y$ , 1/2 −  $z$ . <sup>d</sup> $x$ ,  $y$ ,  $z$ . <sup>e</sup> $x$ , 1 +  $y$ ,  $z$ . <sup>f</sup>1/2 +  $x$ , 3/2 −  $y$ , − $z$ .

ing donor and acceptor groups of these two HBs have components only along  $a$  and  $c$ . As discussed in section 3.4, for the generation of linear susceptibility the role of HB is mainly that of “organizing” the atomic/molecular polarizabilities, which accumulate in the  $ac$  plane. The HB also contributes to a slight enhancement of the atomic polarizabilities along the HB direction, and we can correlate this effect with the augmented bonding electron density. Using the criterion of Espinosa et al.<sup>6p</sup> to evaluate the contribution to the binding energy from the potential energy density at the critical points, we calculate a stabilization of ca. 20 and 25 kcal/mol for the intercation and interanion HBs, respectively (or even 30 kcal/mol using the theoretical density). This gives an idea of the HB energy necessary to perturb the molecular polarizabilities. Noteworthy, while higher electron density in the interanionic O—H⋯O bonds could be anticipated based on the crystal packing and geometries, the stronger influence of the intercationic  $\text{N}_{\text{imidazole}}-\text{H}\cdots\text{O}$  and the lower influence of the interactions between anion and cation are less predictable and they could be quantified only from very accurate electron density measures or calculations.

**3.5.4. Electrostatic Potential.** Electrostatic potential for the L-histidinium and hydrogen oxalate ions was calculated from the experimental charge density<sup>51</sup> in both data sets for different refinement conditions and visualized with MOLISO;<sup>52</sup> see the plots in Figures 12 and 13. The electrostatic potential is important for the study of intermolecular interactions, as it plays a key role in process of molecular recognition, and it is also fundamental for the evaluation of intermolecular interaction energy and the lattice energy.

What is especially interesting here is the zwitterionic nature of L-histidinium. In fact, although it is a cation, it preserves a typical bivalent nature of all neutral zwitterionic amino acids. Of course, the region of positive potential is more extended, but the carboxylate remains slightly negative (or almost zero), regardless of the kind of refinement. The same holds true for the hydrogen oxalate, where the negative potential dominates the external region of the anion but at the proton site, where it is positive. The potential is higher, in absolute values, for the *charge constrained* models, but the distribution of charged regions is almost identical. The two different data sets also offer a possibility to appreciate the experimental uncertainty.

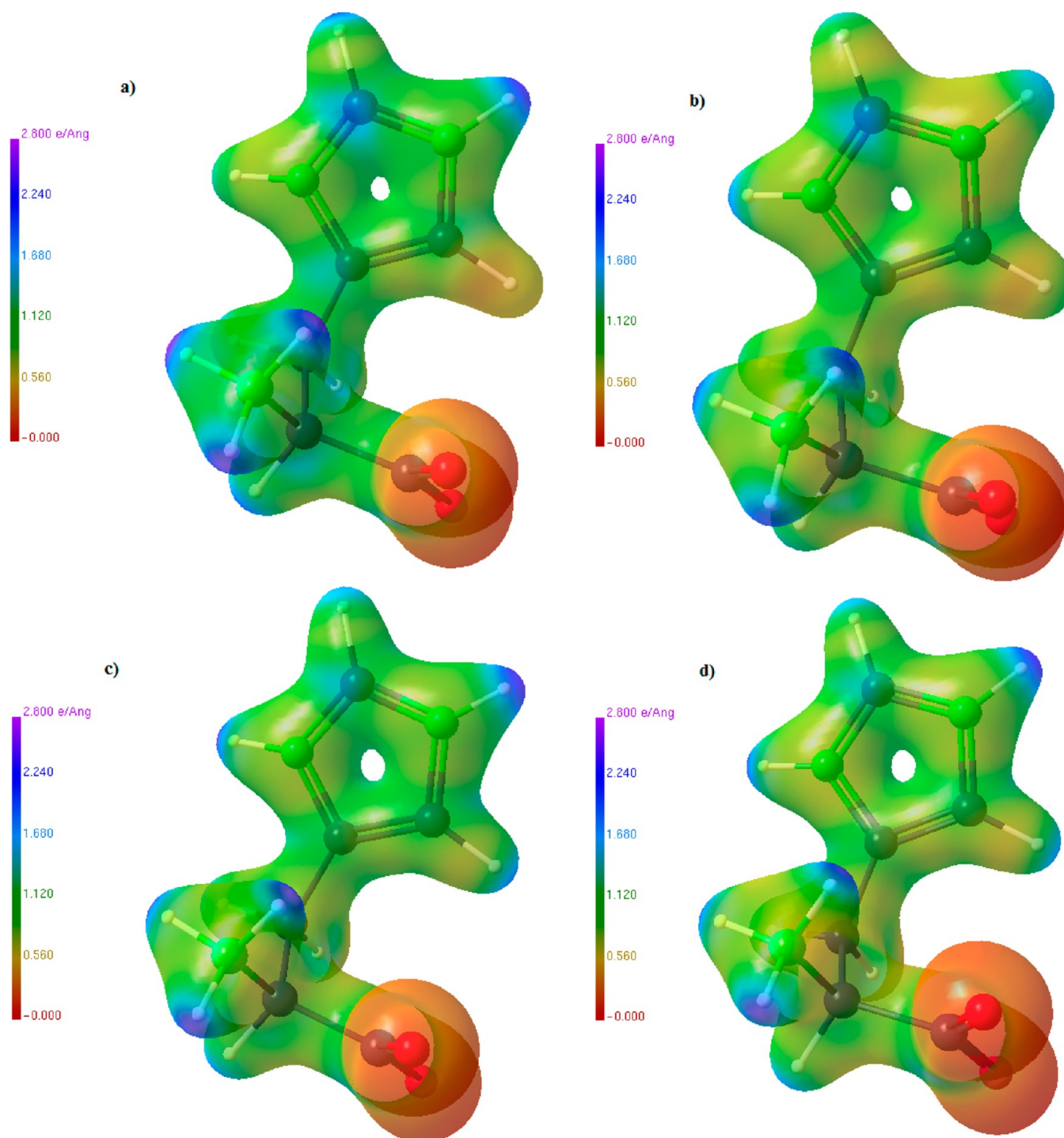


**Figure 12.** The electrostatic potential of *L*-histidinium plotted on a charge density isosurface at  $0.5 \text{ e } \text{\AA}^{-3}$  for (a) 110 K data, charge constraint model; (b) 110 K data, charge transfer model; (c) 100 K data, charge constraint model, (d) 100 K data, charge transfer model. The same color gradient scheme ( $0.0 \text{ e } \text{\AA}^{-1}$  red;  $2.80 \text{ e } \text{\AA}^{-3}$  blue) is used for all plots.

#### 4. CONCLUSIONS

We have analyzed the accurate electron density distribution of *L*-histidinium hydrogen oxalate which belongs to the family of organic salts of amino acids, known for their optical properties and therefore potentially interesting materials. In particular, our purpose was to correlate the measured or calculated refractive indices with the main features of the electron density distribution, focusing on the role of stronger intermolecular interactions.

Using the analysis of the Hirshfeld surfaces, we have shown that the hydrogen bonds have the largest area of influence over the two ions, even though *L*-histidinium has a relatively large side chain which produces also other kinds of (weaker) contacts. The orientation of the strongest hydrogen bonds (i.e., shortest and associated with the largest electron density) is fundamental to explain the particular anisotropy of the optical indicatrix of **1**: the smallest refractive index, in fact, coincides with the direction lacking of strong HBs. However, the HB itself is not dramatically

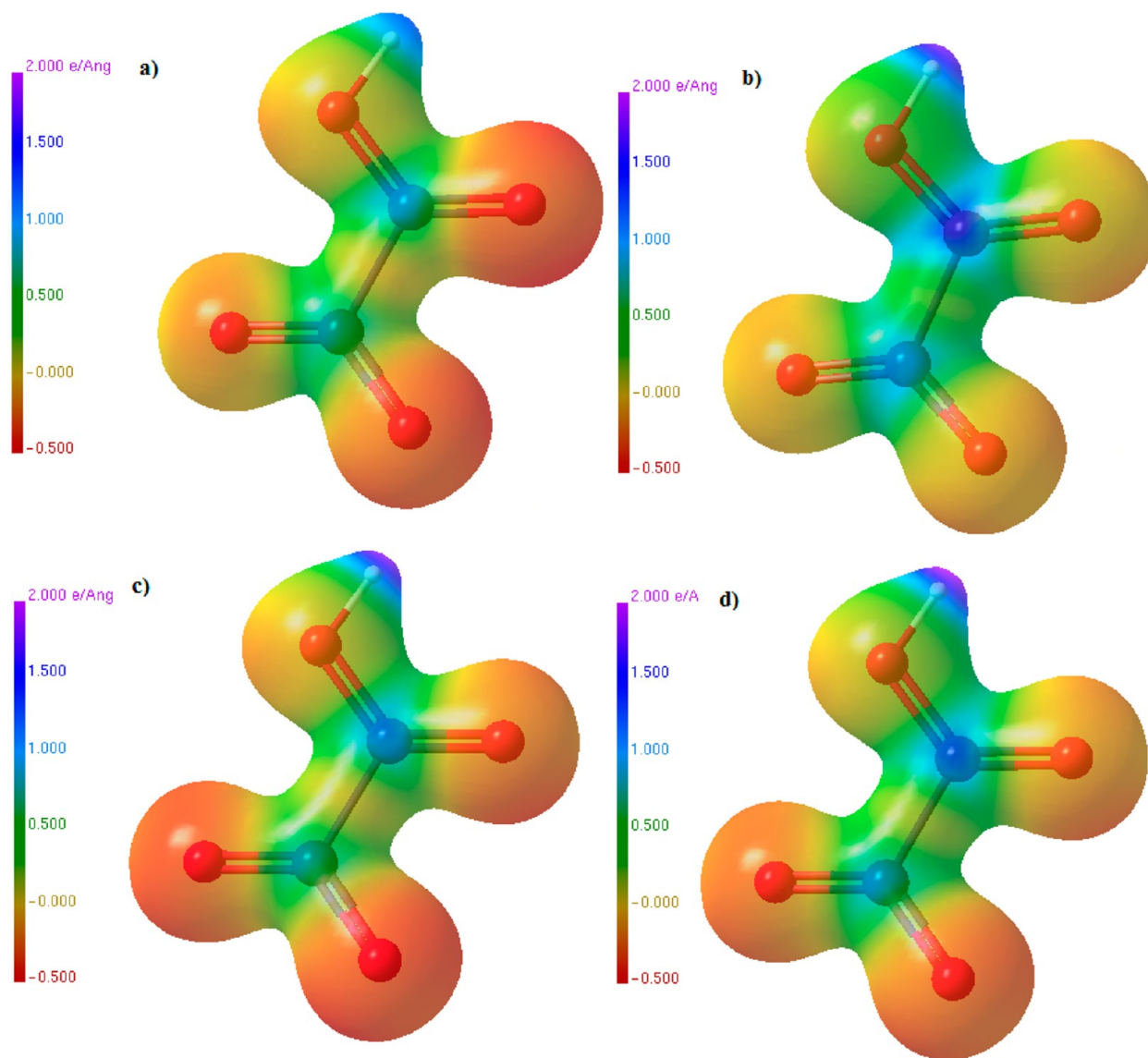


**Figure 13.** The electrostatic potential of hydrogen oxalate plotted on a charge density isosurface at  $0.5 \text{ e } \text{\AA}^{-3}$  for (a) 110 K data, charge constraint model; (b) 110 K data, charge transfer model; (c) 100 K data, charge constraint model; (d) 100 K data, charge transfer model. The same color gradient scheme ( $-0.5 \text{ e } \text{\AA}^{-1}$  red;  $2.0 \text{ e } \text{\AA}^{-3}$  blue) is used for all plots.

affecting the polarizabilities of the two ions; rather its function is to *organize* in space the molecular polarizabilities, by packing the molecules in such a way that they eventually produce a rather large anisotropy. In fact, while the polarizabilities of the HB donor or acceptor atoms are only marginally perturbed even by the strongest HBs, their orientation is determined by the way in which the ions are arranged in the network. In **1**, *a* and *c* are directions along which the atomic tensors of the most polarizable atoms (the oxygen atoms) are larger. Therefore, these two directions are significantly *slower* (higher refractive indices) than *b*, along which the atomic/molecular polarizability tensors have their smallest components.

This study also allowed testing different models of the accurate electron density distribution. The two independent experimental measures, the solid state and the gas phase calculations, were compared and used to scrutinize the results. In particular, we have shown that periodic calculations return accurate positions for H atoms that produce the more sensible modeling against experimental X-ray diffracted intensities, similar to those

obtainable from neutron diffraction or spectroscopic methods. Moreover, the comparison of electrostatic potential surfaces and topological QTAIM analysis showed that treating the ions as rigidly charged is a sufficiently good approximation. This is very important because it means that a rigid treatment of the molecular electronic charge would anyway enable the evaluation of the intermolecular interactions, in particular, if a crystal structure is modeled with sets of multipoles calculated for the isolated ions.

In the future, we plan to extend this kind of analysis to nonlinear optical properties in similar salts or in metal-biomolecular frameworks, based on amino acid and oxalate building blocks. Moreover, we will report on the mechanical properties of **1**, by means of theoretical and experimental crystal structure determinations under pressure.<sup>13</sup>



## ■ ASSOCIATED CONTENT

## ■ Supporting Information

Crystallographic information files; Table S1: PDFT optimized geometry. Figure S1: Probability distribution of residuals. Figure S2: Normal probability plot of residual distribution. Figure S3: Fractal dimension plot. Tables S2–S4: Crystal structure and refinement for L-histidinium bis-hydrogenoxalate, bis-L-histidinium oxalate, and DL-dihistidinium oxalate, respectively. Figures S4–S7: portion of the Hirshfeld surface of histidinium related to O---H close contacts, H---O close contacts, or N---H close contacts, H---N close contacts, respectively. Figures S8 and S9: portion of the Hirshfeld surface of hydrogenoxalate related to O---H close contacts and H---O close contacts, respectively. This material is available free of charge via the Internet at <http://pubs.acs.org>.

## ■ AUTHOR INFORMATION

## Corresponding Author

\*E-mail: [piero.macchi@dcu.unibe.ch](mailto:piero.macchi@dcu.unibe.ch).

## Notes

The authors declare no competing financial interest.

## ■ ACKNOWLEDGMENTS

This work was supported by Swiss National Science Foundation, Project No. 200020\_141271.

## ■ REFERENCES

- (1) Desiraju, G. R. *Angew. Chem., Int. Ed. Engl.* **2011**, *50*, 52–9.
- (2) (a) Gilli, G.; Gilli, P. *The Nature of the Hydrogen Bond: Outline of a Comprehensive Hydrogen Bond Theory*; Oxford University Press: Oxford, UK, 2009. (b) Gilli, G.; Gilli, P. *J. Mol. Struct.* **2000**, *552*, 1–15.
- (3) Jeffrey, G. A., Ed.; *An Introduction to Hydrogen Bonding*; Oxford University Press: Oxford, U.K., 1997.
- (4) Tellgren, R. *Theoretical and Experimental Aspects of the Neutron Diffraction Technique and Its Application to the Study of Ferroelectric and Related Phenomena*; Almquist & Wiksell: Stockholm, 1975.
- (5) Casati, N.; Macchi, P.; Sironi, A. *Chem. Commun.* **2009**, 2679–2681.
- (6) (a) Bindzus, N.; Iversen, B. B. *Acta Crystallogr. A* **2012**, *68*, 750–62. (b) Bytheway, I.; Chandler, G. S.; Figgis, B. N. *Acta Crystallogr. A* **2002**, *A58*, 451–459. (c) Ghanty, T. K.; Ghosh, S. K. *J. Phys. Chem.* **2003**, *107*, 7062–7067. (d) Mata, I.; Alkorta, I.; Molins, E.; Espinosa, E. *ChemPhysChem* **2012**, *13*, 1421–1424. (e) Munshi, P.; Cameron, E.; Guru, R. T. N.; Ferrara, J. D.; Cameron, T. S. *J. Phys. Chem. A* **2007**, *111*, 7888–7897. (f) Nelyubina, Y. V.; Antipin, M. Y.; Lyssenko, K. A. *J. Phys. Chem. A* **2009**, *113*, 3615–3620. (g) Ranganathan, A.; Kulkarni, G. U.; Rao, C. N. R. *J. Phys. Chem. A* **2003**, *107*, 6073–6081. (h) Senthilkumar, L.; Ghanty, T. K.; Ghosh, S. K. *J. Phys. Chem. A* **2005**, *109*, 7575–7582. (i) Steiner, T. *Angew. Chem., Int. Ed.* **2002**, *41*, 48–76. (j) Vener, M. V.; Manaev, A. V.; Egorova, A. N.; Tsirelson, V. G. *Russian J. Phys. Chem. B* **2008**, *2*, 512–524. (k) Vener, M. V.; Manaev, A. V.; Egorova, A. N.; Tsirelson, V. G. *J. Phys. Chem. A* **2007**, *111*, 1155–1162. (l) Wolstenholme, D. J.; Weigand, J. J.; Cameron, E. M.; Cameron, T. S. *Cryst. Growth Des.* **2009**, *9*, 282–290. (m) Macchi, P.; Iversen, B. B.; Sironi, A.; Chakoumakos, B. C.; Larsen, F. K. *Angew. Chem., Int. Ed.* **2000**, *39*, 2719–2722. (n) Ahmed, M.; Jelsch, C.; Guillot, B.; Lecomte, C.; Domagala, S. *Cryst. Growth Des.* **2013**, *13*, 315–325. (o) Liebschner, D.; Jelsch, C.; Espinosa, E.; Lecomte, C.; Chabrière, E.; Guillot, B. *J. Phys. Chem. A* **2011**, *115*, 12895–12904. (p) Espinosa, E.; Molins, E.; Lecomte, C. *Chem. Phys. Lett.* **1998**, *285*, 170–173. (q) Overgaard, J.; Iversen, B. B. *Struct. Bonding (Berlin)* **2012**, *146*, 53–74. (r) Madsen, A. Ø. *Struct. Bonding (Berlin)* **2012**, *146*, 21–52.
- (7) Chimpri, A.; Macchi, P., *in preparation*, 2013.
- (8) Yaghi, O. M.; Li, G.; Li, H. *Nature* **1995**, *378*, 703–706.
- (9) Imaz, I.; Rubio-Martinez, M.; An, J.; Sole-Font, I.; Rosi, N. L.; MasPOCH, D. *Chem. Commun.* **2011**, *47*, 7287–7302.
- (10) Prabu, M. M.; Nagendra, H. G.; Suresh, S.; Vijayan, M. *J. Biomol. Struct. Dyn.* **1996**, *14*, 387–92.
- (11) (a) Petrosyan, A. M.; Sukiasyan, R. P.; Karapetyan, H. A.; Terzyan, S. S.; Feigelson, R. S. *J. Cryst. Growth* **2000**, *213*, 103–111. (b) Petrosyan, A. M.; Karapetyan, H. A.; Sukiasyan, R. P.; Aghajanyan, A. E.; Morgunov, V. G.; Kravchenko, E. A.; Bush, A. A. *J. Mol. Struct.* **2005**, *752*, 144–152. (c) Petrosyan, A. M.; Sukiasyan, R. P.; Karapetyan, H. A.; Antipin, M. Y.; Apreyan, R. A. *J. Cryst. Growth* **2005**, *275*, e1927–e1934. (d) Petrosyan, H. A.; Karapetyan, H. A.; Antipin, M. Y.; Petrosyan, A. M. *J. Cryst. Growth* **2005**, *275*, e1919–e1926.
- (12) Krawczuk-Pantula, A.; Pérez, D.; Stadnicka, K.; Macchi, P. *Trans. Am. Crystallogr. Assoc.* **2011**, 1–25.
- (13) Gao, M.; Chimpri, A.; Macchi, P., to be submitted.
- (14) Macchi, P.; Buerger, H. B.; Chimpri, A. S.; Hauser, J.; Gal, Z. *J. Appl. Crystallogr.* **2011**, *44*, 763–771.
- (15) *CrysalisPRO*, 171.36.20; Agilent Technologies: Yarnton, Oxfordshire, United Kingdom, 2012.
- (16) Sheldrick, G. *Acta Crystallogr. A* **2008**, *64*, 112–122.
- (17) Coppens, P. *X-Ray Charge Densities and Chemical Bonding*; Oxford University Press: Oxford, U.K., 1997.
- (18) Volkov, A.; Macchi, P.; Farrugia, L.; Gatti, C.; Mallinson, P.; Richter, T.; Koritsanszky, T. *XD2006 - A Computer Program Package for Multipole Refinement, Topological Analysis of Charge Densities and Evaluation of Intermolecular Energies from Experimental and Theoretical Structure Factors* 2006.
- (19) Macchi, P.; Coppens, P. *Acta Crystallogr. A* **2001**, *A57*, 656–662.
- (20) Clementi, E.; Raimondi, D. L. *J. Chem. Phys.* **1963**, *38*, 2686–2689.
- (21) (a) Kampermann, S. P.; Ruble, J. R.; Craven, B. M. *Acta Crystallogr. B* **1994**, *50*, 737–741. (b) El Haouzi, A.; Hansen, N. K.; Le Henaff, C.; Protas, J. *Acta Crystallogr. A* **1996**, *52*, 291–301.
- (22) Roversi, P. Ph.D. Thesis, University of Milan, 1996.
- (23) Meindl, K.; Henn, J. *Acta Crystallogr. A* **2008**, *64* (3), 404–418.
- (24) Dovesi, R.; Saunders, V. R.; Roetti, C.; Orlando, R.; Zicovich-Wilson, C. M.; Pascale, F.; Civalleri, B.; Doll, K.; Harrison, N. M.; Bush, I. J.; D'Arco, P.; Llunell, M. *CRYSTAL09*; Università di Torino: Torino, 2009.
- (25) Becke, A. D. *J. Chem. Phys.* **1993**, *98*, S648–S2. Lee, C.; Yang, W.; Parr, R. G. *Phys. Rev. B* **1988**, *37*, 785–789.
- (26) Bonin, K. D.; Kresin, V. V. *Electric-Dipole Polarizabilities of Atoms, Molecules and Clusters*; World Scientific: Singapore, 1997.
- (27) Frisch, M. J.; Trucks, G. W.; Schlegel, H. B.; Scuseria, G. E.; Robb, M. A.; Cheeseman, J. R.; Scalmani, G.; Barone, V.; Mennucci, B.; Petersson, G. A.; Nakatsuji, H.; Caricato, M.; Li, X.; Hratchian, H. P.; Izmaylov, A. F.; Bloino, J.; Zheng, G.; Sonnenberg, J. L.; Hada, M.; Ehara, M.; Toyota, K.; Fukuda, R.; Hasegawa, J.; Ishida, M.; Nakajima, T.; Honda, Y.; Kitao, O.; Nakai, H.; Vreven, T.; Montgomery, J., Jr.; Peralta, J. E.; Ogliaro, F.; Bearpark, M.; Heyd, J. J.; Brothers, E.; Kudin, K. N.; Staroverov, V. N.; Kobayashi, R.; Normand, J.; Raghavachari, K.; Rendell, A.; Burant, J. C.; Iyengar, S. S.; Tomasi, J.; Cossi, M.; Rega, N.; Millam, J. M.; Klene, M.; Knox, J. E.; Cross, J. B.; Bakken, V.; Adamo, C.; Jaramillo, J.; Gomperts, R.; Stratmann, R. E.; Yazyev, O.; Austin, A. J.; Cammi, R.; Pomelli, C.; Ochterski, J. W.; Martin, R. L.; Morokuma, K.; Zakrzewski, V. G.; Voth, G. A.; Salvador, P.; Dannenberg, J. J.; Dapprich, S.; Daniels, A. D.; Farkas, Ö.; Foresman, J. B.; Ortiz, J. V.; Cioslowski, J.; Fox, D. J. *Gaussian09*, A.02; Gaussian Inc: Wallingford, CT, 2009.
- (28) Keith, T. A. *AIMAll*, 12.11.09; TK Gristmill Software: Overland Park, KS, 2012.
- (29) Hartshorne, N. H.; Stuart, A. *Practical Optical Crystallography*; American Elsevier Publishing Co.: Amsterdam, 1969.
- (30) Hinnawi, E. E. *Methods in Chemical and Mineral Microscopy*; Elsevier Publishing Co.: Amsterdam, 1966.
- (31) Spackman, M. A.; Jayatilaka, D. *CrystEngComm* **2009**, *11*, 19–32.
- (32) Wolff, S. K.; Grimwood, D. J.; McKinnon, J. J.; Turner, M. J.; Jayatilaka, D.; Spackman, M. A. *CrystalExplorer*, version 2.1; University of Western Australia: Perth, Western Australia, 2012.
- (33) Spackman, M. A.; McKinnon, J. J. *CrystEngComm* **2002**, *4*, 378–392.



- (34) Glazer, A. M.; Cox, K. G. Classical linear crystal optics. In *International Tables for Crystallography Vol. D: Physical Properties of Crystals*; Authier, A., Ed.; Springer: Netherlands: 2003; Vol. D, pp 150–177.
- (35) (a) Cummins, P. G.; Dunmur, D. A.; Munn, R. W.; Newham, R. J. *Acta Crystallogr. A* **1976**, 32, 847–853. (b) Dunmur, D. A. *Mol. Phys.* **1972**, 23, 109–115.
- (36) Chemla, D. S.; Oudar, J. L.; Jerphagnon, J. *Phys. Rev. B* **1975**, 12, 4534–46.
- (37) (a) Zyss, J.; Berthier, G. *J. Chem. Phys.* **1982**, 77, 3635–53. (b) Hamada, T. *J. Phys. Chem.* **1996**, 100, 8777–8781.
- (38) (a) Wu, K.; Snijders, J. G.; Lin, C. *J. Phys. Chem. B* **2002**, 106 (35), 8954–8958. (b) Balakina, M. Y.; Fominykh, O. D. *Int. J. Quantum Chem.* **2008**, 108 (14), 2678–2692.
- (39) (a) Spackman, M. A.; Munshi, P.; Jayatilaka, D. *Chem. Phys. Lett.* **2007**, 443, 87–91. (b) Whitten, A. E.; Jayatilaka, D.; Spackman, M. A. *J. Chem. Phys.* **2006**, 125, 174505.
- (40) (a) Laidig, K. E.; Bader, R. F. W. *J. Chem. Phys.* **1990**, 93, 7213–7224. (b) Le, S. C. R.; Stone, A. J. *Mol. Phys.* **1993**, 78, 1267–1291.
- (41) Bader, R. F. W. *Atoms in Molecules: A Quantum Theory*; Oxford University Press: Oxford, UK, 1990.
- (42) Keith, T. A. Atomic Response Properties. In *The Quantum Theory of Atoms in Molecules*; Wiley-VCH Verlag GmbH & Co. KGaA: New York, 2007; pp 61–94.
- (43) (a) Spackman, M. A.; Byrom, P. G. *Acta Crystallogr. B* **1996**, 52, 1023–1035. (b) Howard, S. T.; Hursthouse, M. B.; Lehmann, C. W.; Mallinson, P. R.; Frampton, C. S. *J. Chem. Phys.* **1992**, 97, 5616–5630.
- (44) Coppens, P.; Abramov, Y.; Carducci, M.; Korjov, B.; Novozhilova, I.; Alhambra, C.; Pressprich, M. R. *J. Am. Chem. Soc.* **1999**, 121, 2585–2593.
- (45) Song, X.-j.; Rienstra, C. M.; McDermott, A. E. *Magn. Reson. Chem.* **2001**, 39, S30–S36.
- (46) Madsen, A. *J. Appl. Crystallogr.* **2006**, 39, 757–758.
- (47) Koritsanszky, T.; Zobel, D.; Luger, P. *J. Phys. Chem. A* **2000**, 104, 1549–1556.
- (48) Allen, F. H.; Watson, D. G.; Brammer, L.; Orpen, A. G.; Taylor, R., Typical interatomic distances: organic compounds. In *International Tables for Crystallography Vol. C: Mathematical, Physical and Chemical Tables*; Prince, E., Ed.; Springer: Netherlands: 2004; Vol. C, pp 790–811.
- (49) Steiner, T.; Saenger, W. *Acta Crystallogr. B* **1994**, 50, 348–357.
- (50) Cremer, D.; Kraka, E. *Croat. Chem. Acta* **1984**, 57, 1259–1281.
- (51) Volkov, A.; King, H. F.; Coppens, P.; Farrugia, L. J. *Acta Crystallogr. A* **2006**, 62, 400–8.
- (52) Hübschle, C. B.; Luger, P. *J. Appl. Crystallogr.* **2006**, 39, 901–904.